3D strain heterogeneity and fracture studied by X-ray tomography and crystal plasticity in an aluminium alloy

Maryse Gille, Henry Proudhon, Jette Oddershede, Romain Quey, Thilo F. Morgeneyer

3D strain heterogeneity and fracture studied by X-ray tomography and crystal plasticity in an aluminium alloy

Maryse Gille [a,*], Henry Proudhon [a], Jette Oddershede [b], Romain Quey [c], Thilo F. Morgeneyer [a]

[a] MINES Paris, PSL University, Centre des Matériaux, CNRS UMR 7633, BP 87, F-91003 Evry, France

[b] Xnovo Technology ApS, Galoche Alle 15, 1st floor, 4600 Køge, Denmark

[c] Mines Saint-Etienne, Univ Lyon, CNRS, UMR 5307 LGF, F-42023 Saint-Etienne, France

[*] Corresponding author: maryse.gille@minesparis.psl.eu

Abstract

Strong correlations between measured strain fields and 3D crystal plasticity finite element (CP-FE) predictions based on the real microstructure are found for a plane strain tensile specimen made of 6016 T4 aluminium alloy. This is achieved using multimodal X-ray lab tomography giving access to both the initial grain structure and the strain evolution. The real microstructure of the central region of interest (ROI) of the undeformed specimen is obtained non destructively using lab-based diffraction contrast tomography (DCT) and meshing. An *in situ* tensile test, using absorption contrast tomography (ACT) is then performed for twelve loading increments up to fracture. Taking advantage of the plane strain condition, the evolution of the internal strain field is measured by two-dimensional digital image correlation (DIC) in the material bulk using the natural speckle provided by intermetallic particles. Early strain heterogeneities in the form of slanted bands, that are spatially stable over time, are revealed and the fracture path – determined from the *post mortem* scan – is found to coincide with the bands exhibiting maximum strain. CP-FE simulations are performed on the meshed microstructure of the specimen acquired by DCT and are compared with image correlation measurements. The measured strain fields are well described by 3D CP-FE predictions, whilst it is shown that neither a macroscopic anisotropic plasticity model nor a CP-FE simulation with random grain orientations could reproduce the measurements.

Keywords

Correlative X-ray tomography, Diffraction contrast tomography, Polycrystal, Plane strain tension, Crystal plasticity finite element simulation

1. Introduction

In light of the current need to reduce CO_2 emissions and improve fuel efficiency, light weight structural materials are increasingly used by automakers (Watarai, 2006). Aluminium alloys are thus more and more considered in the automotive industry to replace steel. For both inner and outer automotive panels, formability is of particular interest for manufacturers who want to produce complex geometries, including sharp edges, together with a good surface finish (Ota et al., 2020). While formability of steel has already been significantly optimized, there are now new challenges for optimizing the formability of the aluminum alloys that may replace steel in future automotive body panels. The standard tool to evaluate part feasibility in terms of stamping performance of a metal is the forming limit curve (FLC), which consists of mapping the conditions for the onset of necking (plastic localization) in terms of principal strains for stress states ranging from uniaxial to equi-biaxial tension, following the procedure prescribed by ISO norms (International Organization for Standardization, 2008a, 2008b). In FLCs, the critical strain state for formability is the lowest point in terms of major strain. It corresponds to plane strain with the minor strain being near zero (Holmberg et al., 2004). By definition, in the plane strain state, deformation only occurs in a 2D plane (Kelly, 2013). Most

automotive stamping failures occur near plane strain and William G. Brazier has found out that it concerns 85 % of stretching failures in automotive stampings (Ayres et al., 1978). The plane strain state is thus of particular interest, and several lab tests like V-bending or Limiting Dome Height are used to assess metal sheet formability in this particular strain state. Several studies have focused on the development of easy-to-perform plane strain tensile tests with various specimen geometries (Holmberg et al., 2004; Park et al., 2020; Granum et al., 2021; Gille et al., 2024). Single crystal deformation experiments under plane strain boundary conditions have proved valuable in elucidating the role played by such constraints in the formation of deformation textures during rolling and drawing (Hartley and Kysar, 2020).

Stress triaxiality defined as $\eta = \sigma_m/\sigma_{eq}$ with σ_m the hydrostatic stress and σ_{eq} the equivalent Von Mises stress was shown by several authors to have an impact on material strength (Lou et al., 2020) and on fracture mechanisms (Thomason, 1990; Pineau et al., 2016). At high levels of triaxiality, the higher the triaxiality, the lower the fracture strain. However, the fracture strain does not increase monotonically with decreasing triaxiality (Bao and Wierzbicki, 2004; Papasidero et al., 2015). Despite the inconsistency of studies, the literature indicates that there are complex relations between triaxiality, Lode angle and fractures strain. Some authors have highlighted the importance of the Lode angle parameter $\bar{\theta}$, which, when close to 0, means lower ductility of the material. Thus, fracture strain can be represented as a surface depending on both η and $\bar{\theta}$ on which plane strain tension – even if not in high stress triaxiality ($\eta = 1/\sqrt{3}$) – is in the lowest part of the surface as the Lode angle parameter $\bar{\theta} = 0$ (Mohr and Marcadet, 2015; Papasidero et al., 2015)

In the last decades, 4D X-ray imaging techniques have significantly developed both at synchrotron sources and in laboratory tomographs, enabling deformation and damage mechanisms to be visualized up to failure by applying a mechanical loading with a dedicated *in situ* loading device (Maire and Withers, 2014; Wu et al., 2017; Proudhon et al., 2020; Xiao et al., 2024). Image correlation techniques applied on absorption contrast tomography (ACT) scans enable local internal strain fields to be measured both in 2D with digital image correlation (DIC) (Sutton et al., 2009) and in 3D with digital volume correlation (DVC) (Bay et al., 1999; Bornert et al., 2004; Roux et al., 2008). In some studies, markers were introduced inside the material to provide the contrast required for registration (Bornert et al., 2004; Haldrup et al., 2008). However, additional markers may affect the mechanical behaviour of the material, so for this study, it was decided to rely on the natural speckle provided by inherent intermetallic particles, as image correlation had already been successfully performed on aluminium alloys with similar particle contents (Buljac et al., 2018; Morgeneyer et al., 2014, 2016, 2021). In these experimental studies, strain fields were measured in the plane strain zone ahead of a localizing notch of a compact tension specimen revealing various strain heterogeneity mechanisms. In AA2198 T8R, a single early localization band was observed at the location of final slanted fracture (Buljac et al., 2018; Morgeneyer et al., 2014), whereas in AA2139 T3 and AA7075 T651, several bands were found to compete at early steps, before localization and fracture occurred on one or two of these initial bands (Morgeneyer et al., 2021, 2016). However, there are currently no studies that report experimentally observed strain heterogeneity within the bulk of an aluminium alloy deformed in plane strain tension.

The polycrystalline effects on strain heterogeneities have been explored in several studies by combining surface DIC and Scanning Electron Microscopy (SEM) / Electron BackScattered Diffraction (EBSD) techniques (Héripré et al., 2007; Tasan et al., 2014; Rotella et al., 2021; Bean et al., 2022; Pelligra et al., 2022). However, only the surfaces of the specimens were observed with these methods without considering the mechanisms occurring in the core of the samples, that can be far from the plane stress conditions of the surface. This was overcome by Morgeneyer et al. (2021), who used 3D imaging techniques to measure the internal strain field in the plane strain state region ahead of the notch of a

compact tension-like specimen. The experimental strain field was compared with a simulated strain field obtained with a 2D plane strain crystal plasticity finite element (CP-FE) simulation performed on a microstructure constructed from EBSD data. Similar strain heterogeneities were found experimentally and numerically, but a one-to-one comparison was not possible. The microstructure used for the CP-FE simulation was indeed measured on the same material but on a region different from the one where DIC was performed as the acquisition of such an EBSD would have been acquired *post mortem*. Similarly, by coupling destructive 3D EBSD and numerical simulation, Sarmah et al. (2024) found that the role of grains in damage growth in a 7075-O aluminium alloy was negligible compared to particle decohesion and cracking. Singh et al. (2019) also used CP-FE simulation on EBSD data to investigate the micromechanical deformation behaviour of three magnesium alloys during mini-V-bending test.

The development of diffraction contrast tomography (DCT), first at synchrotrons (Ludwig et al., 2008; Johnson et al., 2008) and then in laboratory tomographs (Bachmann et al., 2019; Oddershede et al., 2022; Ganju et al., 2023; Nieto-Valeiras et al., 2024), now makes it possible to non-destructively measure the 3D microstructure of a specimen with grain morphology and crystallographic orientations for the undeformed state. For example, Kobayashi et al. (2022) mapped the microstructure of an undeformed Al-Cu alloy specimen by lab-based DCT before acquiring *in situ* ACT scans, taking advantage of microstructural feature tracking to obtain the 3D local strain field. They showed that early strain heterogeneities are related to final strain localization. The grain size, shape and orientation effects were investigated, but no obvious conclusion could be drawn. It was found that grain neighborhood plays a major role in strain heterogeneity, making strain evolution a very complex problem that might be understood using CP-FE simulations. Another recent study combined lab-based DCT, CP-FE simulations and *in situ* ACT to investigate the effects of microstructure on void growth (Vaughan et al., 2024). They found no clear relationship between the void growth rate and the crystallographic orientations of the neighboring grains.

Historically, 3D finite element simulations relying on CP-FE constitutive equations have been based on synthetic microstructures that could be generated based on texture measurements (Barbe et al., 2001; Ghorbanpour et al., 2020; Sedighiani et al., 2021). More recently, CP-FE simulations were applied to experimental spatially-resolved microstructures acquired by DCT or three-dimensional X-ray diffraction (3DXRD) and deformed to a few percent strain (Proudhon et al., 2011; Rovinelli et al., 2020; Renversade and Quey, 2024). CP-FE results have already been compared to experimental results obtained by image correlation, but this was limited to surface analysis (Héripré et al., 2007; Zhao et al., 2008; Tasan et al., 2014; Lin et al., 2020).

The objective of this paper is to study strain heterogeneity and strain localization and how this affects the final fracture path for a 6016 T4 aluminium alloy deformed in plane strain tension. Polycrystalline effects on the strain heterogeneity have been investigated thanks to 3D CP-FE simulations based on the real microstructure. The material, the plane strain tensile specimen and the *in situ* tomography setup for acquisition of DCT and ACT scans are described in section 2, whilst section 3 describes the numerical procedure applied for performing CP-FE simulations on the measured microstructure. Measured and simulated internal strain fields are then presented in section 4 before being discussed in section 5 to investigate strain heterogeneity mechanisms and the role of crystallography in strain localization and final fracture. Finally, a conclusion is presented in section 6.

2. Experimental procedure

2.1. Material

The specimen was made of 6016 T4 aluminium alloy provided by Constellium C-TEC as a 1.15 mm thin sheet. For the purpose of this academic study requiring a stabilized material, the AA6016 T4 metal

sheet was naturally aged for more than one year and is supposed to have retained stable mechanical properties. AA6016 is used for outer automotive body panels and is optimized for formability, with silicon and magnesium as main alloying elements. The chemical composition is detailed in Table 1.

Element	Si	Mg	Fe	Mn	Cu	Zn	Ti	Cr
wt%	1.0-1.5	0.25-0.6	≤ 0.50	≤ 0.20	≤ 0.20	≤ 0.20	≤ 0.15	≤ 0.10

Table 1 – Chemical composition limits of AA6016 in weight percentage (wt%) (The Aluminum Association, 2018)

Figure 1.a) shows the grain structure of the material on a volume acquired by lab-based DCT as described in the following. Processing directions are referred to as L for the rolling direction, T for the transverse direction and S for the short-transverse direction (thickness direction). The material, which was recrystallized, showed equiaxed grains with an average equivalent diameter of 40 µm and a moderate Cube-type texture (see Figure 1.b). A 2D section of a high-resolution ACT scan is displayed in Figure 1.c). It shows the different constituents of the alloy, which are revealed by their different densities and thus X-ray absorption. The volume fraction of intermetallic particles (appearing in white) was measured to be 0.64 % by segmenting the 3D scan, while the volume fraction of voids (in black) is about 0.1 %.

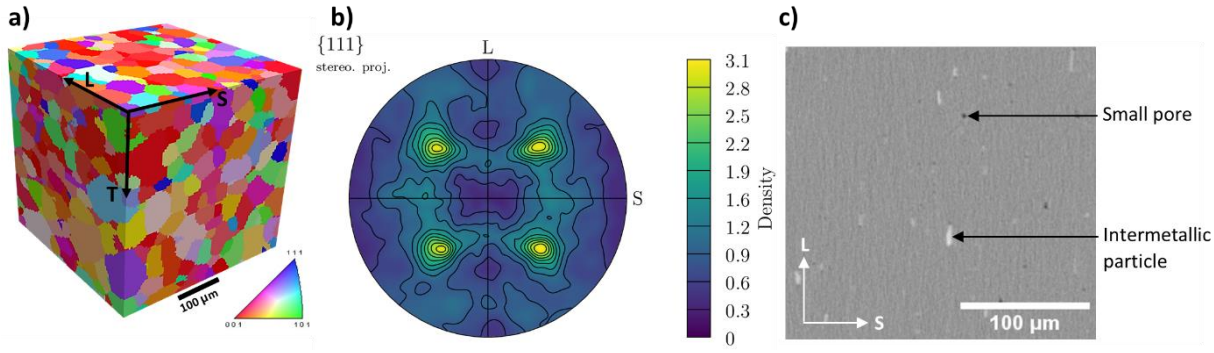

Figure 1 – Material microstructure: a) T-axis Inverse Pole Figure showing the 3D grain structure acquired via lab-based DCT; b) {111} pole figure; c) 2D slice of a high-resolution ACT scan acquired by lab tomography

Relevant mechanical parameters are given in Table 2. The material is very ductile (high strain at fracture) with strong work hardening ($Rm/Rp_{0.2}$ = 2). The anisotropy in stress is very low but the anisotropy in strains is not negligible as indicated by the r-values, also called Lankford coefficients (Lankford et al., 1950).

E (GPa)	in transverse direction			r_0	r_{45}	r_{90}
	$Rp_{0.2}$ (MPa)	Rm (MPa)	A (%)			
71	115	232	28	0.83	0.45	0.67

Table 2 – Mechanical properties of AA6016 T4

2.2. Miniaturized plane strain tension specimen and mechanical test

Since the study required the proper capture of grains and intermetallic particles, the characteristic size of which was around ten microns, high-resolution tomography was the appropriate technique, but it necessitated the miniaturization of the plane strain tensile specimen. Full-thickness specimen geometries with wide ROI, like the one proposed by Granum et al. (2021), was therefore unsuitable and a flat grooved specimen geometry, inspired by publications from Bai et al. (2009) and Park et al. (2020), was chosen as a compromise. This design led to elastic deformation only in the thick part of the

specimen during tension, thereby preventing deformation in the width direction (referred to as the Y direction in Figure 2.a). So, the center of the specimen remained close to the plane strain state.

In order to meet both the plane strain requirement and size requirement enabling micrometer-scale imaging by tomography, an optimal specimen geometry was determined using finite element calculations based on a macroscopic anisotropic Barlat-type model proposed by Bron and Besson (2004) and parameters identified as described in section 3.1 and appendix A. A criterion was set for the plane strain condition. Namely, the ratio of strain in the tension direction, Z, to the strain in the Y direction (perpendicular to the tension axis) should be higher than 10 all along the loading path. This condition was numerically found to be achieved for a specimen with a region of interest (ROI) of a width of 4 mm, a height of 0.6 mm and a thickness of 0.5 mm, which was also compatible with CT characterizations. The selected miniaturized plane strain tension specimen design can be seen on Figure 2.a. Figure 2.b shows the sample machined by electrical discharge machining (EDM), so that the tension direction is the transverse direction of the metal sheet T. Appendix B presents the experimental verification of the plane strain state in the center of the specimen by DIC on the surface of the specimen.

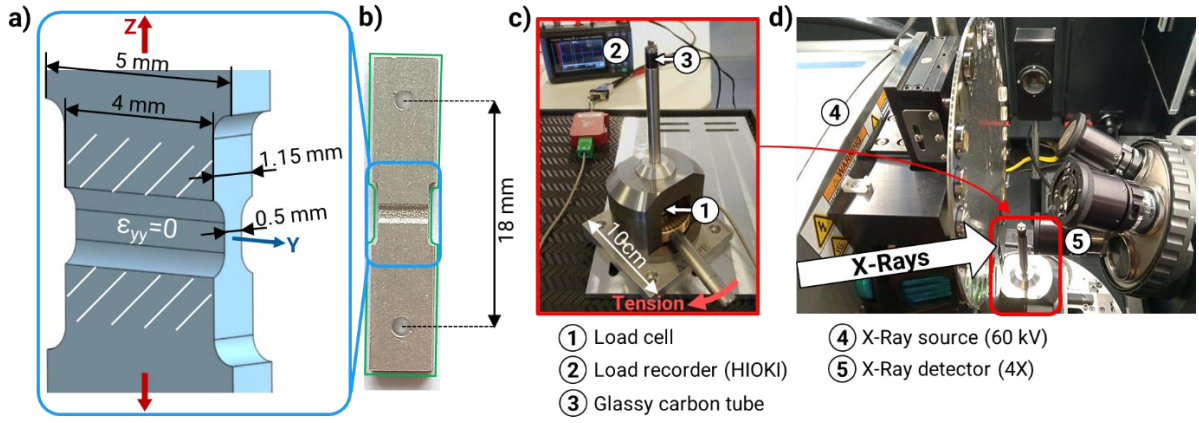

Figure 2 – a) Dimensions of the ROI of the miniaturized plane strain tension specimen and b) picture of a machined specimen; c) manual in situ *tension setup called* Statix *and d) ACT setup*

A dedicated *in situ* tension device called *Statix* (shown in Figure 2.c) was developed so as to apply the loading steps to the specimen. As shown on Figure 2.d, *Statix* was sufficiently compact to fit in the lab tomograph and provides a sample-to-source distance of 12 mm. The load was applied manually by means of a handle linked to a loading screw which transmitted the mechanical load via a load cell and a long grip to the sample. The sample was maintained in the stress rig by means of two pins and a glassy carbon tube was used to carry the load to the frame whilst ensuring 360° X-ray visibility without hindering the absorption.

2.3. Lab tomography (DCT and ACT)

The 3D non-destructive imaging of the specimen was performed on a ZEISS Xradia 520 Versa lab tomograph equipped with a lab-based DCT module. A DCT scan and 14 ACT scans were collected following the steps presented in Figure 3.

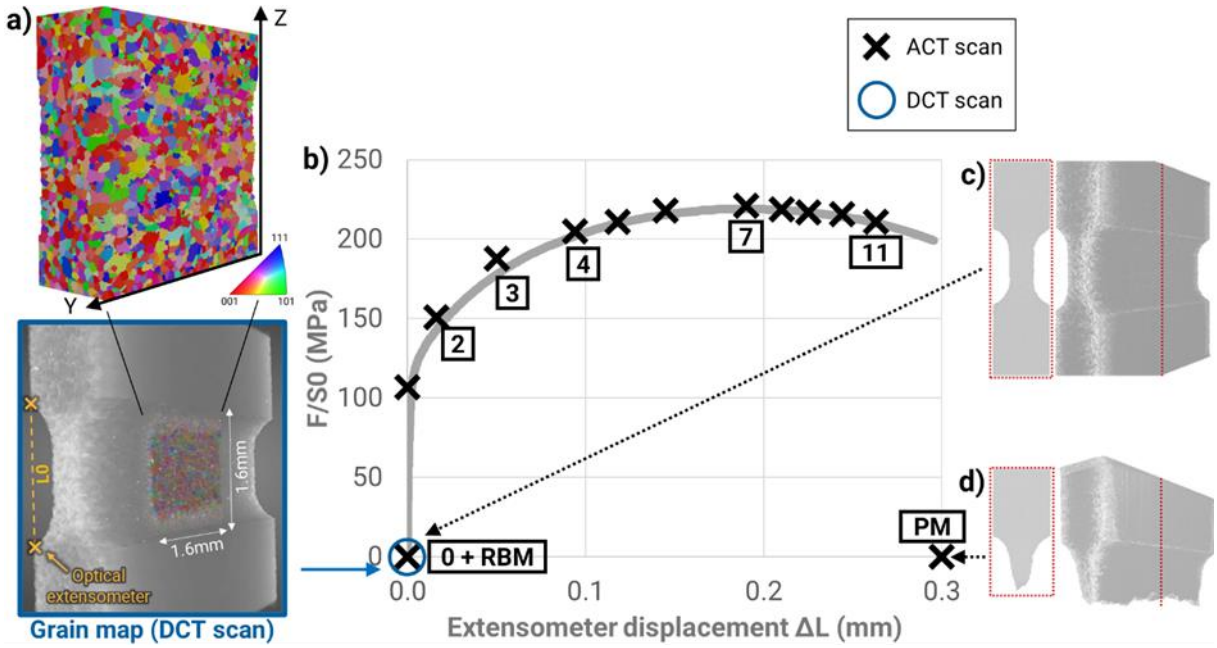

Figure 3 – Stress-displacement curve of the plane strain tensile test showing the distribution of tomography scans acquired during the in situ *test: a) Grain map of the central ROI of the undeformed specimen acquired by lab-based DCT, b) engineering stress vs optical extensometer displacement with position of the different tomography scans, c) ACT scan of the undeformed specimen and d) ACT scan of the upper half of the* post mortem *specimen*

The undeformed specimen was first scanned by lab-based DCT outside of the *Statix* setup to obtain the crystallographic orientations and morphologies of the grains in the ROI. A polychromatic divergent beam with an acceleration voltage of 110 kV and a power of 9 W was used. The DCT data was collected in projection geometry with the sample placed 14 mm from the source and 246 mm from the flat panel CMOS detector. To constrain the beam onto a limited illuminated volume in the sample, an aperture of size 375 × 375 µm² was used. A beamstop of 20 × 20 mm² was placed between the sample and the detector to block directly transmitted X-rays and enhance the diffraction signals. The Helical Phyllotaxis HART acquisition strategy adapted to plate-like specimens was used (Oddershede et al., 2022). In total, 1792 diffraction projections were collected with an exposure time of 60 s and no binning. The DCT scan was reconstructed using the Xnovo Technology GrainMapper3D™ 3.1 software (Bachmann et al., 2019), resulting in a volume of 400 × 400 × 138 voxels of a size of 4 µm.

ACT scans were then acquired in the lab tomograph, taking advantage of the contrast provided by the presence of intermetallic particles and pores in the material. For the ACT scans, an acceleration voltage of 60 kV and a power of 4 W were used. The setup, which uses the 4X detector, is visible on Figure 2.d. For each loading step, two scans with different resolutions were obtained: an overview scan with resolution 4.5 µm/pixel, to determine the precise specimen geometry and measure displacement with an optical extensometer; and a high-resolution scan with resolution 0.8 µm/pixel, for correlation, as detailed in section 2.5. The parameters of the two configurations are provided in Table 3.

To evaluate the uncertainty of displacement measurements by DIC, the undeformed specimen was scanned twice at both resolutions, with a vertical rigid body motion (RBM) of approximately 300 µm performed between the scans.

	Overview scan	High-resolution scan
Sample to source distance	26mm	12mm
Sample to detector distance	13mm	39mm
Binning	2	1
Exposure time	2s	12s
Number of projections	1601	3201
Voxel size	4.5µm	0.8µm

Table 3 – Acquisition parameters of the two configurations for ACT scans

2.4. Alignment of DCT and ACT scans

To ensure perfect alignment between the DCT and ACT scans, an image registration procedure was performed. This is crucial when the goal is to carry out FE simulation based on the DCT polycrystal image, and to compare the results to the strain field measured by image correlation based on the ACT scans. To achieve this, we leveraged a comparison of the DCT and ACT data with EBSD and SEM imaging data of the sectioned post-mortem sample. This ultimately enabled a direct correlation of the measured grain map with the internal strain field obtained by p-DIC.

The registration procedure involved the following steps, as illustrated in Figure 4:

- 1: First, one-half of the *post mortem* specimen was sectioned in the region of the DCT-ROI, polished to a mirror-like quality and observed with two different techniques in a Nova NanoSEM 450 SEM leading to Figure 4.a images. A backscattered-electron (BSE) image was acquired with a voltage of 5 kV, revealing both the specimen surface roughness and the location of intermetallic particles, whilst the grains and their orientations were obtained with multi-field EBSD mapping carried out at 15 kV with a working distance of 12 mm. Indexation was performed with a step of 2 µm, which provided both an inverse pole figure (IPF) revealing grain orientations and an image quality (IQ) image on which the (non-diffracting) intermetallic particles are visible.
- 2: Second, distortions between EBSD and BSE images were corrected by registering EBSD IQ and BSE images using the Fiji bUnwarpJ plugin (Arganda-Carreras et al., 2006; "bUnwarpJ," 2020). Some manually determined landmarks were added as inputs relying on surface roughness and intermetallic particles.
- 3: Third, the Y-normal slice in the ACT *post mortem* scan corresponding to the section imaged by SEM was located in the scan, as shown in Figure 4.b. Subsequently, the registration between BSE image and ACT slice was performed using the Fiji bUnwarpJ plugin (Arganda-Carreras et al., 2006; "bUnwarpJ," 2020). (To increase visibility of intermetallic particles, a 2D projection of the maximum grey level along the Y direction, in a 20 voxels – i.e. 16 µm – thick volume, was used for the ACT scan.)
- 4: Then, the Y-normal slice in the ACT scan of the undeformed specimen corresponding to the SEM-imaged cut was located (see Figure 4.c) using the intermetallic particles present both in the *post mortem* scan and in the initial scan of the undeformed specimen. The displacement field between the undeformed and the *post mortem* specimen was measured using the Fiji bUnwarpJ plugin (Arganda-Carreras et al., 2006; "bUnwarpJ," 2020).
- 5: Next, the displacement field identified from step 1 to 4 was applied to the EBSD IPF image using again the Fiji bUnwarpJ plugin (Arganda-Carreras et al., 2006; "bUnwarpJ," 2020). Thus, the grain information provided by the EBSD IPF image was given in the frame of the ACT scan of the undeformed sample, as can be seen on Figure 4.d.
- 6: Further, based on the assumption that grains in the thicker area of the specimen were hardly deformed during the tensile test, the two scans (ACT and DCT) of the undeformed specimen

were aligned along the Y direction, by finding the slice in DCT scan corresponding to the grains visible in EBSD IPF. The determined slice in DCT scan is visible in Figure 4.f.

- 7: Finally, the offsets between EBSD IPF image and DCT cut in X and Z directions were determined by minimizing mean square error in IPF colour space. The superposition of the EBSD and DCT data after alignment is shown in Figure 4.g.

Note that Fiji bUnwarpJ plugin (Arganda-Carreras et al., 2006; "bUnwarpJ," 2020) was only used for the alignment of DCT and ACT scans and was not involved in the deformation analysis. Deformation was measured by a commercial DIC code on projected 3D data (see section 2.5). Results are presented in section 4.1.

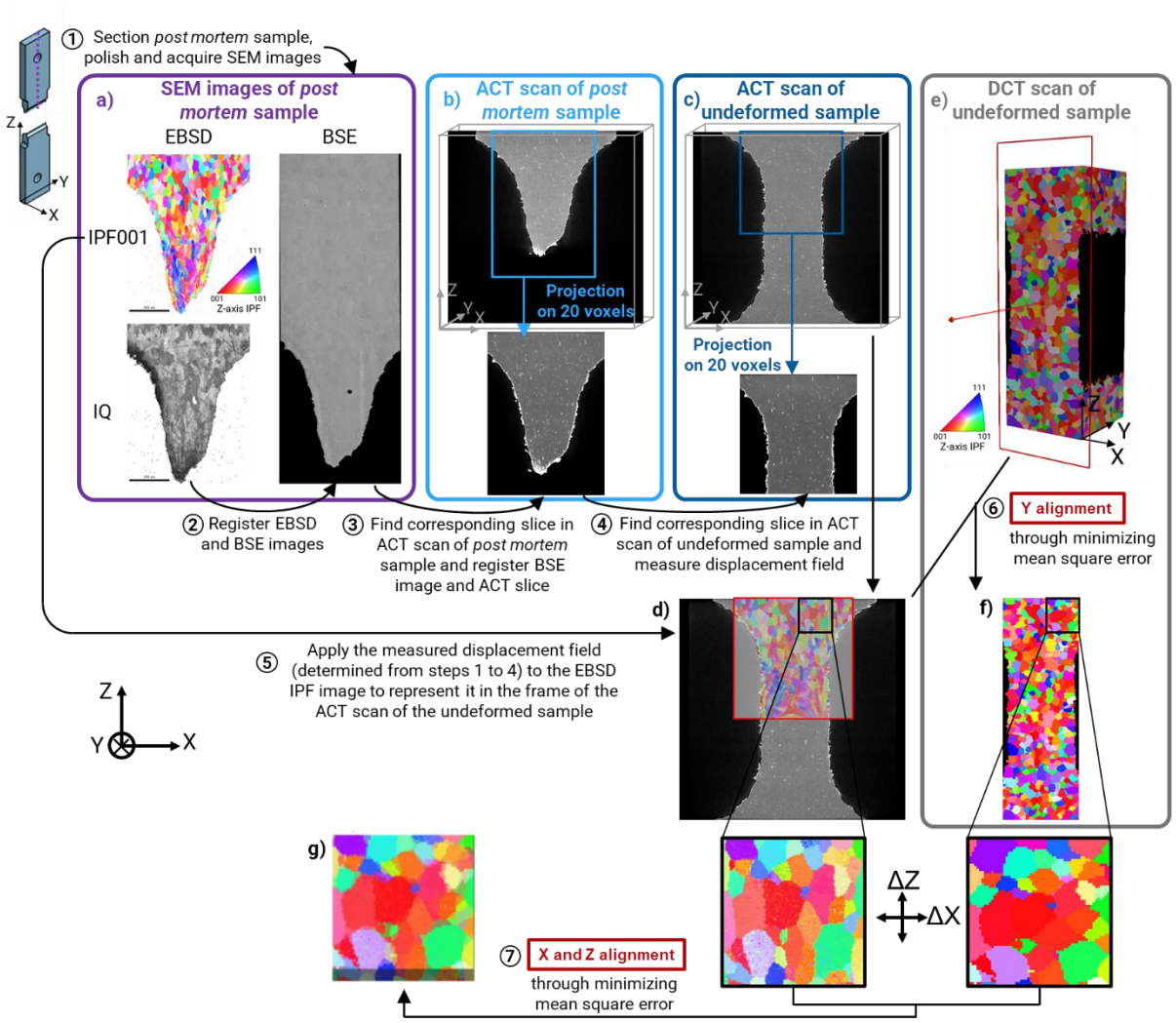

Figure 4 – Methodology applied for the alignment registration of DCT and ACT scans of the undeformed specimen: a) SEM images (EBSD and BSE) of a cut in the post mortem *specimen are used and registered to b) the corresponding slice in the ACT scan of the* post mortem *sample and to c) the corresponding slice in the ACT scan of the undeformed sample; this leads to d) the EBSD IPF data in the frame of the ACT scan of the undeformed sample. ΔY alignment is found by identifying the f) DCT slice corresponding to EBSD IPF data of the* post mortem *cut and g) ΔX and ΔZ alignments are determined by minimizing mean square error between EBSD IPF and DCT data*

2.5. Projection digital image correlation (p-DIC)

The aim of this study is to compare measured strain field inside the material to CP-FE simulations of the real microstructure obtained by DCT and meshing. Ideally, i.e. if enough 3D image contrast was present and if the strain increments were small enough, we could use DVC to measure the full 3D strain field. However, the intermetallic particles only appeared with low contrast (small volume fraction, 0.64 %) in the aluminium matrix (c.f. Figure 1.c), which made it very difficult to perform DVC. Alternatively, taking advantage of the plane strain condition along the width (Y axis) in the centre of the specimen, it was therefore decided here to use the "projection-DIC" (p-DIC) procedure, validated by Buljac et al. (2018) by comparison with DVC measurements. As shown on Figure 5.a, this method consisted in projecting the maximum grey level (i.e. closest to white and corresponding to intermetallic particles) found in a 3D volume onto a 2D image to enhance the contrast compared to a single 2D section of the tomography scan. Several projection distances from 20 to 50 voxels were investigated. The lowest projection distance providing sufficient contrast to obtain meaningful correlation results was found to be 40 voxels corresponding to 32 µm, which represented slightly less than the average grain size. This p-DIC technique also offered the advantage of reducing the negative effect of damage on correlation. Nucleation and growth of porosities indeed violate the hypothesis of grey level conservation required for DIC. By projecting the maximum grey value (i.e. close to white), the porosities (which are black in the 3D scan) did not appear on the 2D projection and thus did not affect correlation. The drawback of p-DIC was that only a 2D strain field could be obtained (in the material bulk) and not the full 3D field.

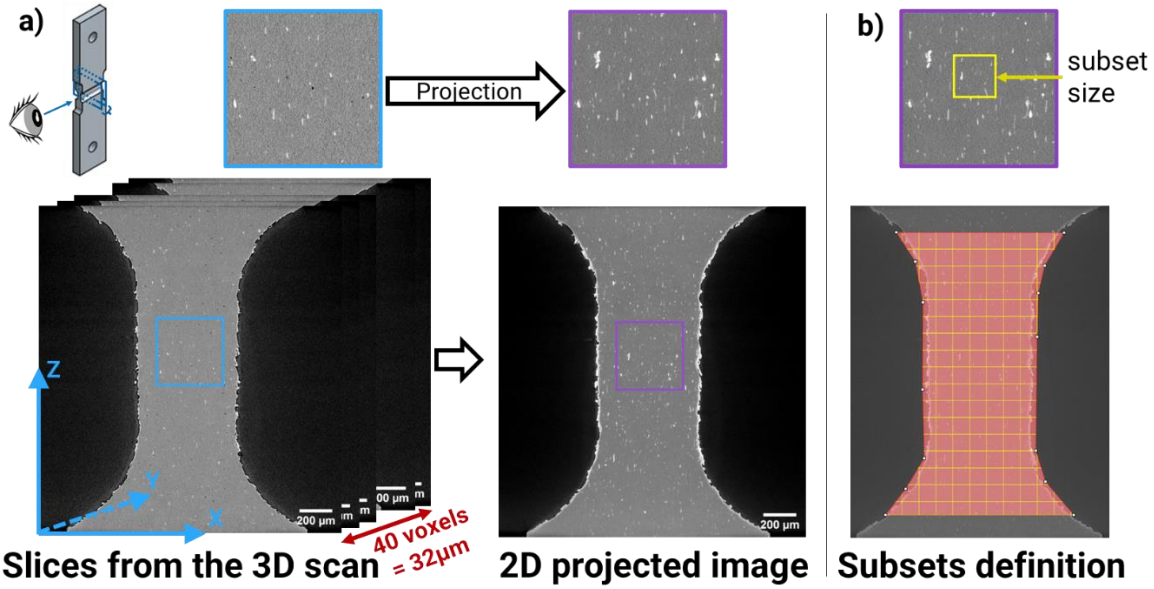

Figure 5 – a) Projection-DIC method of bright contrast (particles) in the reconstructed scan along the plane strain direction illustrated on the initial ACT scan for the undeformed sample; b) Subset size utilized for DIC: 101 pixels = 81 µm

2D local DIC was conducted on the 2D projected images, using the commercial software Vic-2D 7 (Correlated Solutions) to measure the internal displacement and strain fields in the specimen. Because the specimen was highly deformed, correlation was performed incrementally. Specifically, each image was compared to the previous image rather than to the reference image. A subset size of 101 pixels (81 µm) and a step size of 3 pixels (2.4 µm) were chosen; the subsets can be visualized on Figure 5.b. Hencky strain was computed with a 15 x 15 Gaussian smoothing (36 µm).

The measurement noise was evaluated by performing correlation on two projected images obtained from two distinct scans of the same undeformed specimen separated by a vertical rigid body displacement of approximately 300 µm. By applying the previously described DIC procedure, homogeneous vertical and lateral displacement fields of average values of 307 µm and 0.7 µm were measured, respectively, corresponding to the applied vertical rigid body motion. The strain standard deviation was found to be 0.7 %, indicating that the measured strain values were too noisy to measure elastic deformations, but were valid for the (large) plastic deformations of interest in this work.

3. Numerical procedure

All the numerical simulations presented in this article were conducted using the Z-set FE code (Z-set, 2022).

3.1. Macroscopic anisotropic plasticity model

An initial simulation of the specimen with a macroscopic model was performed. It will be called "specimen simulation" for the rest of the article. Since the material presented an anisotropic plastic behaviour, the same model as Kong et al. (2023) with the yield function proposed by Bron and Besson (2004) was used. Equations of the model and identification of the parameters are detailed in appendix A. A view of the mesh composed of linear hexahedral elements (c3d8) with selective integration is visible on Figure 7.a. The finite strain formalism was used, and a displacement of 0.6 mm was applied between the pins with a speed of 0.002 mm/s.

3.2. Crystal plasticity framework

Aluminium being a FCC metal, cubic elasticity was considered, and plasticity could be explained at the crystal scale by dislocation sliding among its 12 octahedral slip systems. The morphology and mean orientation of each grain of the polycrystalline aggregate was known from the DCT scan. A finite element calculation could thus be performed on the meshed microstructure with known lattice orientation providing the initial value of the Schmid tensor $\underset{\sim}{N}^s$ defined for each slip system s as:

$$\underset{\sim}{N}^s = \underline{l}^s \otimes \underline{n}^s$$

with $\underline{l}^s$ the slip direction and $\underline{n}^s$ the vector normal to the slip system

A Meric-Cailletaud CP-FE model was chosen for this work (Méric et al., 1991). The finite strain formalism was used as the material is strained beyond 5 %. The multiplicative decomposition of the deformation gradient $\underset{\sim}{F}$ into an elastic part $\underset{\sim}{E}$ and a plastic part $\underset{\sim}{P}$ was thus considered:

$$\underset{\sim}{F} = \underset{\sim}{E}.\underset{\sim}{P}$$

The resolved shear stress τ^s acting on a given slip system s was determined by the Schmid law:

$$\tau^s = \underset{\sim}{M} : \underset{\sim}{N}^s$$

where $\underset{\sim}{M}$ is the Mandel tensor defined as:

$$\underset{\sim}{M} = \underset{\sim}{E}^T.\underset{\sim}{E}.\underset{\sim}{\Pi}^e$$

$\underset{\sim}{\Pi}^e$ is the second Piola-Kirchhoff stress tensor:

$$\underset{\sim}{\Pi}^e = det(\underset{\sim}{E})\ \underset{\sim}{E}^{-1}.\underset{\sim}{\sigma}.\underset{\sim}{E}^{-T}$$

where $\underset{\sim}{\sigma}$ is the Cauchy stress tensor.

An elastoviscoplastic behaviour with nonlinear isotropic hardening and kinematic hardening was considered.

The plastic slip rate $\dot{\gamma}^s$ is related to the resolved shear stress via a Norton law:

$$\dot{\gamma}^s = \left\langle \frac{|\tau^s - x^s| - r^s}{K} \right\rangle^n sgn(\tau^s - x^s)$$

where K and n are two material viscosity parameters. Macaulay brackets $\langle \dots \rangle$ describe a ramp function which only keeps the positive part.

The cumulated plastic slip rate $\dot{v}^s$ is expressed as follows:

$$\dot{v}^s = |\dot{\gamma}^s|$$

x^s is the kinematic hardening expressed as follows:

$$x^s = c\alpha^s$$

$$\dot{\alpha}^s = \dot{\gamma}^s - d\alpha^s \dot{v}^s$$

where d is the hardening speed and c/d the hardening capacity.

r^s is the isotropic hardening expressed as follows:

$$r^s = \tau_0 + \mathrm{Q} \sum_{r=1}^{12} h_{rs}\left(1 - e^{-bv^r}\right)$$

where v^r is the cumulated plastic slip on system r, τ_0 the critical resolved shear stress, Q the hardening capacity, b the hardening speed and h_{rs} the interaction matrix with six independent variables $h_1, h_2, \dots, h_6$.

3.3. Choice of material parameters

The three independent terms of the stiffness tensor were taken from the work of Vallin et al. (2004) who determined the elastic constants of aluminium at ambient temperature (300 °K) to be $C_{11} = 107.3\ GPa$, $C_{12} = 60.8\ GPa$ and $C_{44} = 28.3\ GPa$.

As the identification of the coefficients of the interaction matrix h_{rs} is both difficult and time-consuming, it was decided to use the coefficients presented in Table 4. They were adapted from the results of dislocation dynamics simulations carried out by Madec and Kubin (2017) for aluminium by only keeping three different values to account for the error in such simulations.

h_1	h_2	h_3	h_4	h_5	h_6
1.0	1.0	0.6	2.3	1.0	1.0

Table 4 – Values of the interaction matrix coefficients

The parameters τ_0, Q and b of the isotropic hardening law, c and d of the kinematic hardening law as well as K and n of the viscosity Norton law were identified using the Z-opt optimization module of the Z-set FE code. Han (2012) found out that a polycrystalline aggregate comprising a sufficient number of cubic grains with random crystallographic orientations representative of the material provided an acceptable estimate of the homogenized behaviour of a representative elementary volume. It was therefore decided to identify parameters by minimizing the difference between experimental uniaxial tensile data and simulated response of a polycrystalline aggregate representative of the material at two different strain rates: $\dot{\varepsilon} = 1.\,10^{-3}\ s^{-1}$ and $\dot{\varepsilon} = 2.5.\,10^{-4}\ s^{-1}$. Reduced quadratic hexahedral elements

(c3d20r) were used for the simulation. A convergence analysis both in terms of number of grains and number of elements per grain was carried out leading to the choice of an aggregate of 125 cubic grains (5 x 5 x 5) with 8 elements per grain (2 x 2 x 2). This led to the identified values presented in Table 5. The material parameters identification is detailed in appendix C.

τ_0	Q	b	c	d	K	n
45.32	21.80	14.21	384.96	33.86	5.67	3.70
MPa	MPa	-	MPa	-	$MPa.s^{1/n}$	-

Table 5 – Identified material parameters

Viscosity parameters were found to be low values corresponding to the low strain rate sensitivity observed on the experimental data. It was also verified that kinematic hardening only helped to accurately capture the experimental behaviour without significantly outweighing isotropic hardening. The kinematic hardening contribution indeed represented 10 MPa. Note that two isotropic hardenings instead of the {isotropic + kinematic} formulation would have also worked and yield similar results.

3.4. 3D CP-FE mesh and simulation

Given the very large number of grains inside the sample, and to limit the size of the CP-FE simulations, it was decided to work on (3D) subvolumes with a thickness of 60 voxels (corresponding to 240 µm or six grains) along the Y direction, centred on specific slices of interest. Meshes of the microstructure were obtained using the open-source software Neper, following the general methodology described in Refs. (Quey et al., 2011; Quey and Renversade, 2017) and illustrated in Figure 6 for the subvolume located about slice y2 (as will be defined in Figure 8). The procedure to go from the DCT image of the full microstructure to a viable mesh of a subvolume involved several steps. Starting from the full DCT image of the polycrystal (Figure 6.a), the smallest grains (containing less than 27 voxels, i.e. with an equivalent diameter lower than 15 µm) were first removed, and the resulting voids were then simply filled by geometrical growth of the adjacent grains. The removed grains can be considered sufficiently small that they would not have influenced the main properties of the deformation field. A Laguerre tessellation was then obtained from the microstructure, which closely approximated the shapes of the grains (Figure 6.b). This was primarily done to later facilitate meshing, but it also allowed the filtering of any imperfections in the grain shape definition that might result from the experimental characterization. The full tessellation was then cut around the slice of interest (Figure 6.c and f). The smallest grains (containing less than 27 voxels) resulting from the cutting were again removed, and regularization was applied to remove the smallest edges and faces of the tessellation (Figure 6.d). Altogether, this allowed us to obtain a mesh of the microstructure comprised of high-quality quadratic tetrahedral elements (c3d10) (Figure 6.e and f), which was then used in CP-FE simulations. It was verified on the 125-grain polycrystal used for material calibration that the quadratic hexahedral elements (c3d20r) and the quadratic tetrahedral elements (c3d10) led to the same simulated mechanical response.

Both the intermetallic particles and voids were intentionally not meshed. The aim of the study was indeed to investigate the effects of grains, which was made possible here by dissociating them from the effects of intermetallic particles and voids. Furthermore, several considerations suggest that the particles and voids have very little effect on the strain heterogeneity. This is at least the result of a study which compared two 2D CP-FE simulations with and without the presence of elastic particles (Morgeneyer et al., 2021). Besides, damage measurements in the core of the specimen have shown that damage is quite low and only increases after the maximum load (see appendix D) meaning that its role in the strain heterogeneity onset was negligible.

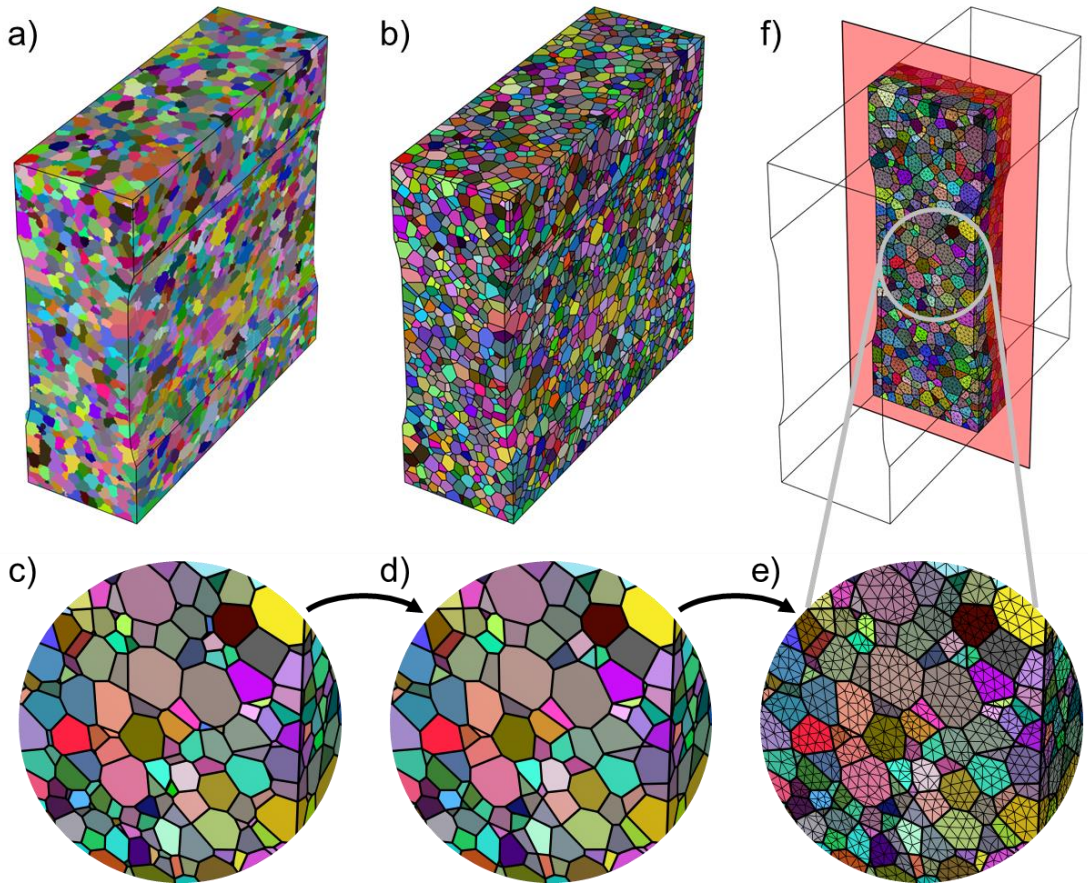

Figure 6 – Meshing methodology illustrated for the polycrystalline aggregate around slice y2 (see Figure 8) using Neper (Quey et al., 2011; Quey and Renversade, 2017). (a) full DCT image of the polycrystal and (b) corresponding tessellation. Zoom illustrating the various intermediate steps: (c) cropped tessellation about the slice of interest, (d) cleaned and regularized tessellation, and (e) meshed subvolume. This results in the (f) final meshed subvolume about the slice of interest (shown in red)

The boundary conditions applied to the FE mesh are described in Figure 7. To ensure that the conditions applied in the polycrystal deformation simulation were as close as possible to the experimental ones for the considered specimen shape, a "submodel" method was used. The method consists of using a simulation of the deformation of the entire plane strain specimen (the "specimen simulation") to determine the boundary conditions of the submodel simulation (the "polycrystal simulation"). The "specimen simulation" was carried out using a macroscopic plasticity model. The displacements on the boundary nodes of the "polycrystal simulation" were then obtained by interpolation from the displacements of the "specimen simulation". More specifically, for faces "A" (see Figure 7.b), the Y displacements were imposed, which corresponded to the near plane strain condition, while the X and Z displacements were left free. This allowed for the development of strain heterogeneities at the grain scale, which would not have been possible if all components of the displacement field were imposed. For faces called "B", all X, Y and Z displacements were imposed from the "specimen simulation". Finally, the faces where specimen thickness was reduced were left free, consistently with the experimental conditions.

As presented in appendix E, it was verified that the central ROIs of the three simulated polycrystalline aggregates around y1, y2 and y3 satisfied the fixed plane strain criterion: $|\varepsilon_{zz}/\varepsilon_{yy}| > 10$.

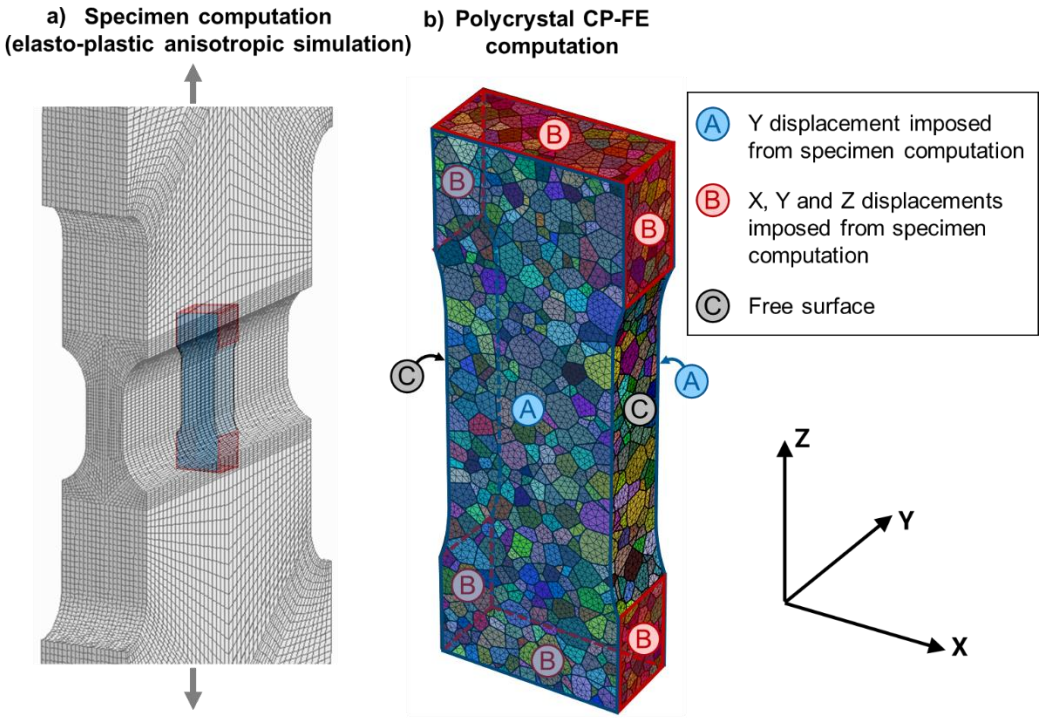

Figure 7 – Definition of the boundary conditions for the CP-FE simulation on the polycrystalline aggregate: a) a FE simulation with macroscopic anisotropic plasticity model on the full plane strain specimen was used to provide displacements to be imposed on the b) submodel polycrystal CP-FE boundary nodes.

4. Results

4.1. Experimental strain field evolution and comparison with macroscopic anisotropic plasticity model simulation results

The evolution of the internal strain fields was investigated with the p-DIC technique (described in section 2.5) on three different sections located, as can be seen in Figure 8 in the central region of the specimen that was verified to be close to plane strain state. Slice y1 is located 284 µm from the central slice on the negative side and sections y2 and y3 are, respectively, located 59 µm and 398 µm from the central slice on the positive side. Figure 8 presents the evolution of the Hencky ε_{zz} strain field along the tensile direction for five steps of the *in situ* test and their correlation with the location of the final fracture, which was determined from the *post mortem* scan.

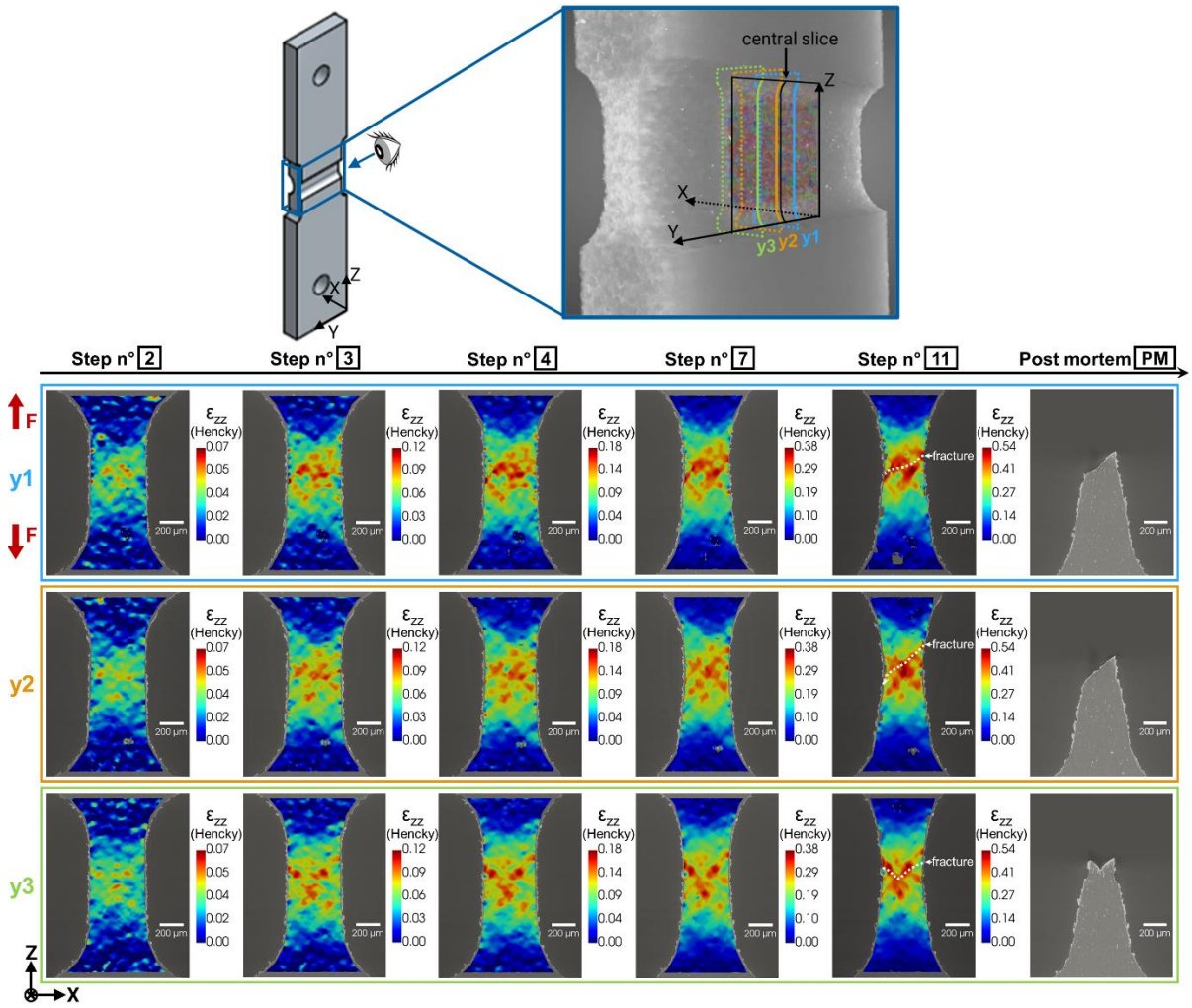

Figure 8 – Evolution of the internal accumulated strain field along the loading direction, ε_{zz}, measured by projection-DIC compared to the location of final fracture determined with the post mortem *scan for 3 sections located in the plane strain region of the specimen. The Hencky strain fields are displayed in the deformed configuration.*

As soon as plasticity set in, that is to say from ACT scan number 2 (see location on mechanical curve in Figure 3), a heterogeneous strain field was measured with p-DIC. In the three investigated sections, the early strain heterogeneities remained stable spatially during the experiment and the location of the maximum strain was consistent with final fracture location. Strain heterogeneities appeared in form of slanted strained bands that competed with each other before strain localized on one or more of them. On section y1, three slanted bands oriented towards the upper left and two slanted bands oriented towards the upper right were visible at early stages. The strain then localized on the two slanted bands oriented towards the upper right with fracture occurring on a path connecting these two bands. For section y2, three slanted bands oriented towards the upper left and three slanted bands oriented towards the upper right competed with a similar intensity. Fracture finally occurred along a path linking the two upper slanted bands oriented towards the upper right. For section y3, several bands can be seen, but two bands forming a "V" emerge from the early stages and strain localization as well as fracture follow this V-shaped path, thereby showing the clear link between early strain heterogeneity and final crack path.

In Figure 9, strain heterogeneities are examined in more detail for section y2 using line profiles. The figure shows the evolution of ε_{zz} Hencky strain along a white and a cyan line on this section. The strain

profiles measured by p-DIC were directly compared with the corresponding strain profiles obtained from a numerical simulation using a Bron-Besson material model (Bron and Besson, 2004).

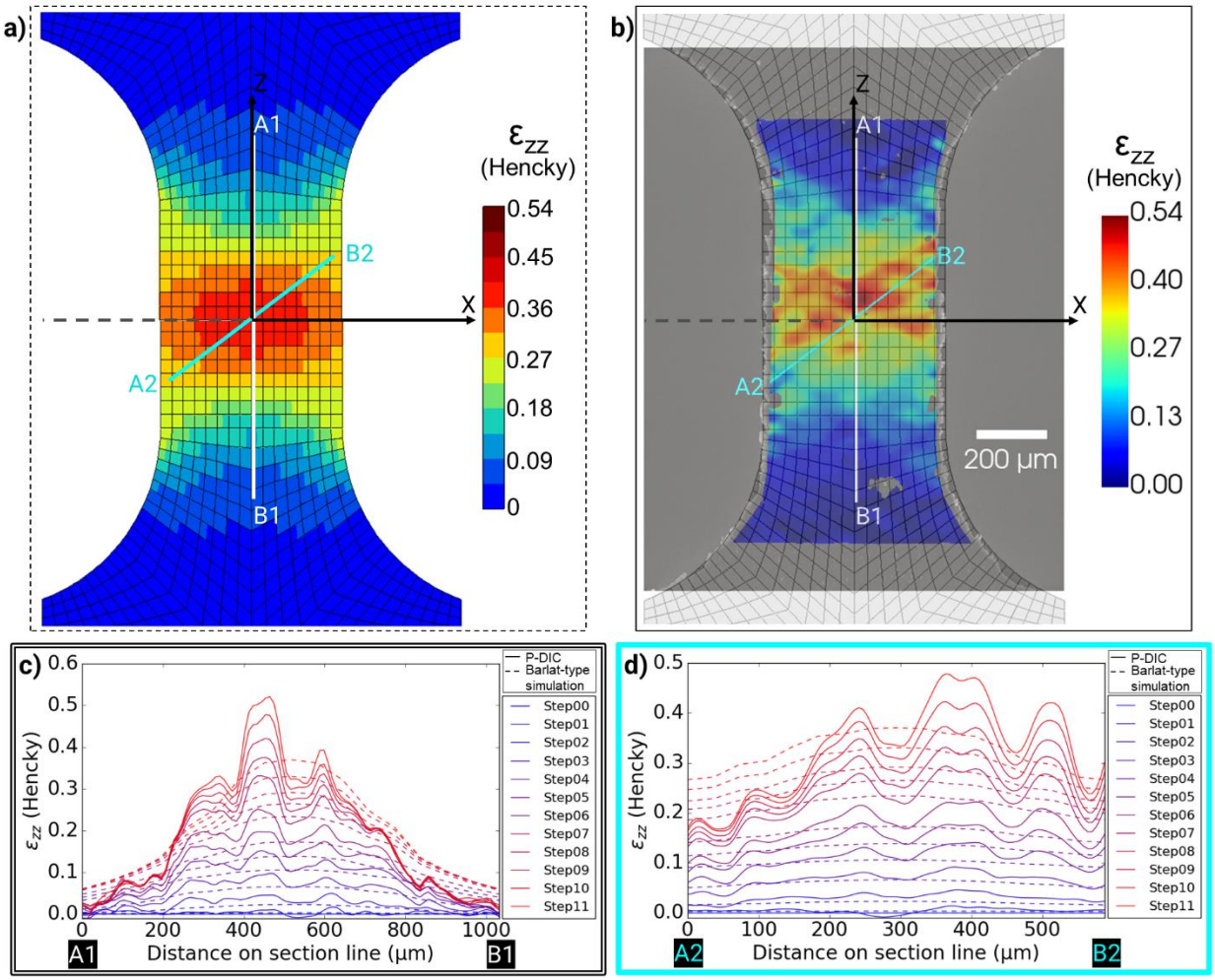

Figure 9 – Comparison of the ε_{zz} field obtained by a) macroscopic anisotropic simulation and b) p-DIC measurement at step 11 in reference configuration for slice y2. A white and a cyan line profiles are defined and their locations are displayed on a) and b); A comparison of the evolution of ε_{zz} measured by p-DIC (solid line) and simulated with a Bron-Besson model (dashed line) is presented along c) the white line profile and d) the cyan line profile.

From step 2, i.e. from the start of plasticity, the strain profiles measured by p-DIC were heterogeneous with local maxima corresponding to the bands observed in Figure 8. These bands remained stable in space during the entire loading history. They had a width of 70-80 µm and were separated by 100 to 150 µm. This is to be compared with the material characteristics but also to the p-DIC parameters. The band widths were thus similar to twice the average grain size of 40 µm but also to the subset size of 81 µm used for correlation. The interpolated strain field data were nonetheless obtained with a resolution of 2.4 µm corresponding to the correlation step size so the comparison with the grain size seems relevant.

The out-of-band strain level was slightly lower than the strain simulated with Bron-Besson behaviour whilst the in-band strain level was significantly higher. Overall, the ε_{zz} strain ratio inside and outside the bands was such that: $\frac{\varepsilon_{zz}^{inside\ band}}{\varepsilon_{zz}^{outside\ band}} \in [1.2,1.7]$. This ratio was lower than those of 2 and later 2.5-3 found by Morgeneyer et al. (Morgeneyer et al., 2021) but this may have been due to the present use

of Hencky strain, which is logarithmic, unlike the Green-Lagrange strain used in the study of Morgeneyer et al. Also, the strain measure noise was estimated to 0.7 % for one step but as incremental correlation was used here, the error may be cumulated meaning that 0.007 would be a lower estimate of the measurement error.

The measured strain heterogeneities were not reproduced by the macroscopic anisotropic plasticity model simulation which encourages further investigation on the effects of the grain structure.

4.2. Comparison with strain field from CP-FE calculation

3D CP-FE simulations were performed following the method described in section 3. The strain fields in the polycrystalline aggregates around the previously defined slices y1, y2 and y3 were compared to the p-DIC measurements as can be seen on Figure 10.

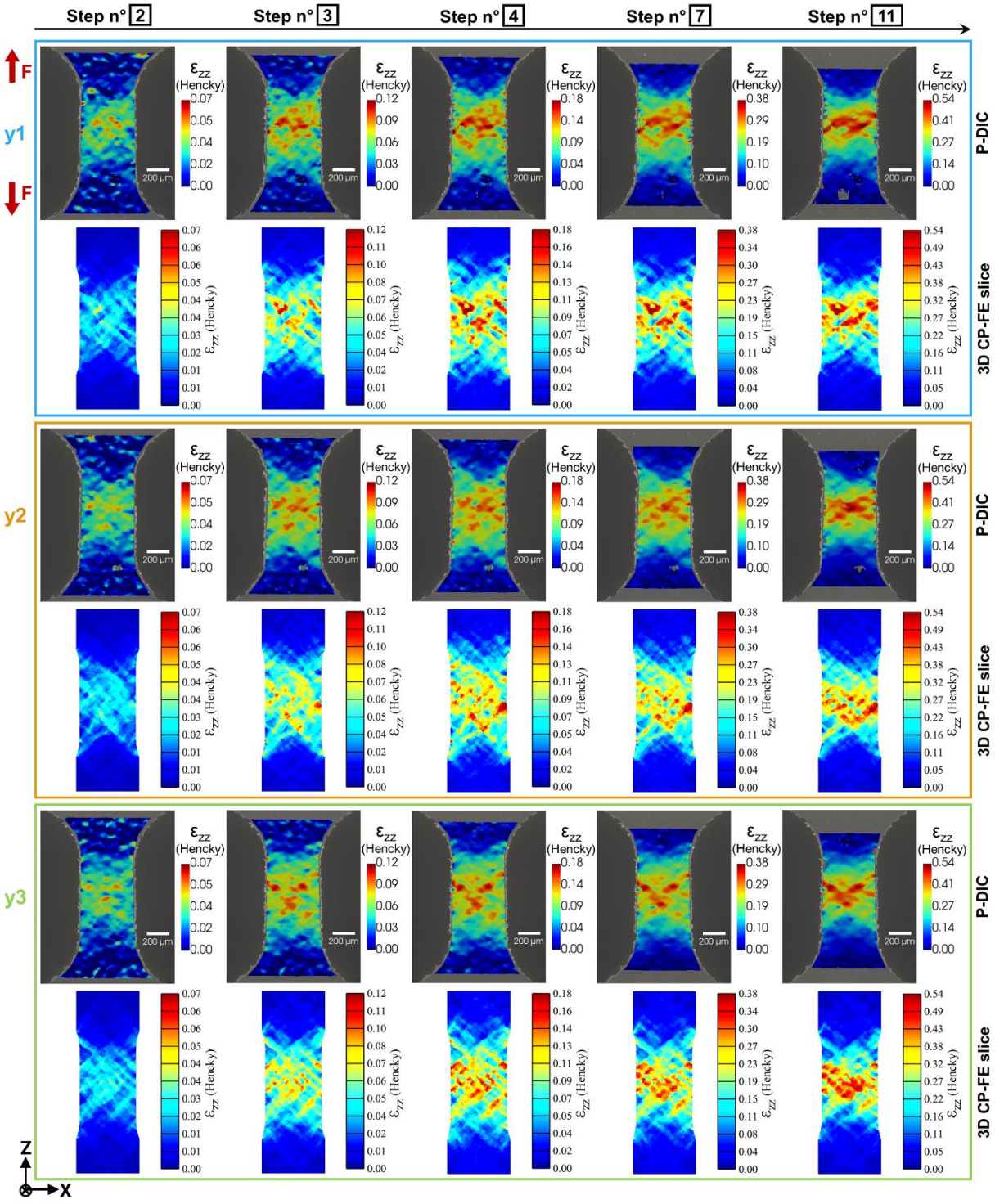

Figure 10 – Comparison of the evolution of the internal accumulated strain field ε_{zz} in loading direction measured by p-DIC and calculated with 3D CP-FE simulations for the three sections y1, y2 and y3. The Hencky strain fields are displayed in the reference configuration.

CP-FE simulations predicted strain heterogeneities of the same magnitude as those measured with p-DIC. The location of "hot spots" were also in good agreement between the measured and simulated strain fields, especially for slices y1 and y3. For slice y1, the strain heterogeneity obtained with the CP-FE simulation was similar to the one obtained with p-DIC measurements. For slice y2, the simulated strain heterogeneity pattern was similar to the one measured at early steps with similar strain bands. However, for this slice, strain localization did not occur at the same location between the simulation

and the measurement. The reasons for this are unclear but may relate to the approximations made to generate a mesh of the microstructure in this specific region. For slice y3, the V-shaped area where strain was measured to be maximum and to coincide with the fracture location was well predicted in the CP-FE simulation. Some other less active strain bands were also found to coincide p-DIC and CP-FE simulation results.

To investigate the strain heterogeneities further, the strain fields obtained by CP-FE simulation and measured by p-DIC were compared along profile lines as can be seen on Figure 11 for slice y3.

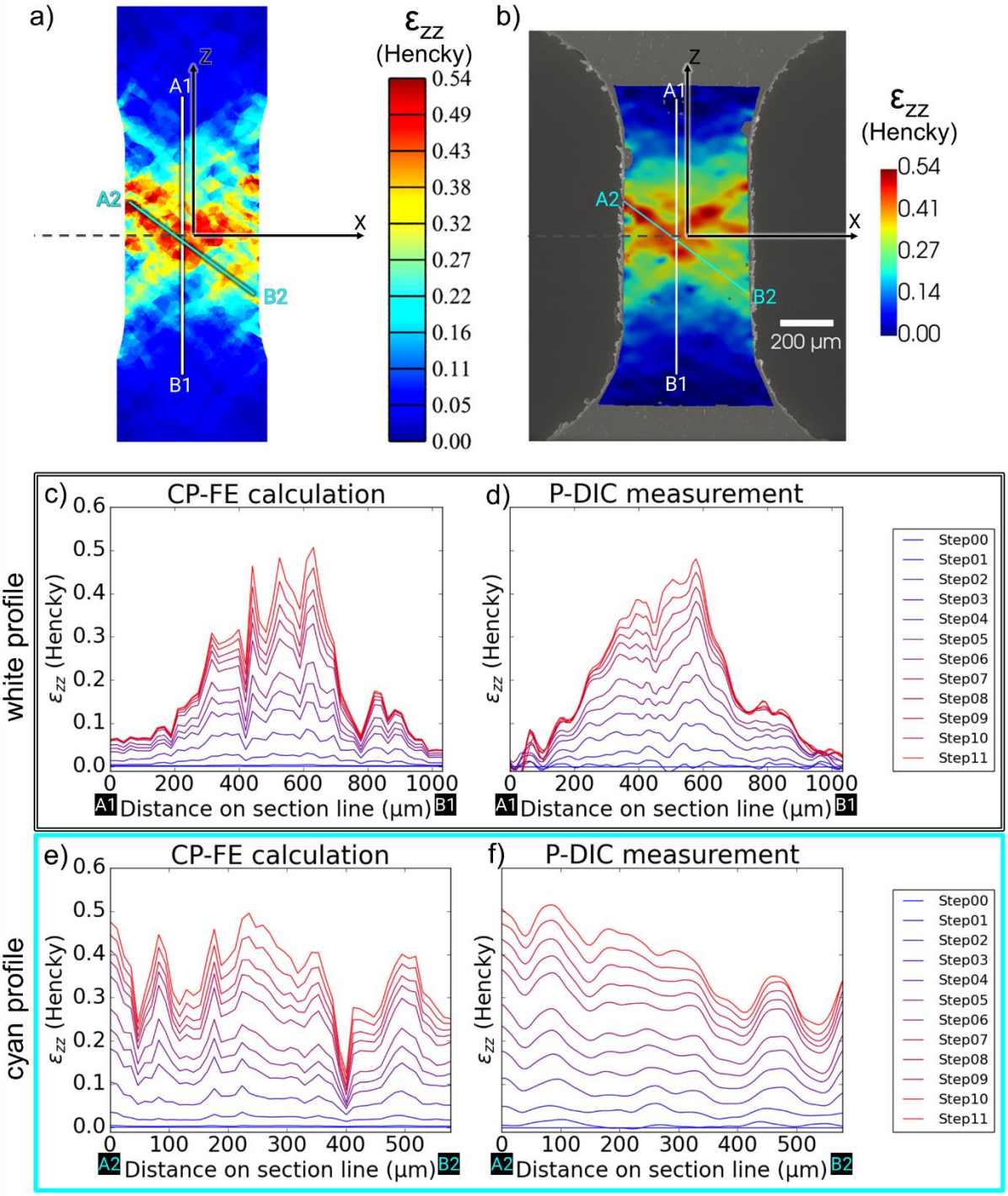

Figure 11 – Comparison of the accumulated ε_{zz} field along the loading direction obtained by a) CP-FE simulation and b) p-DIC measurement at step 11 in the reference configuration for slice y3. A white and a cyan line profiles are defined and their locations are displayed on a) and b). A comparison of the

evolution of ε_{zz} on the white profile is presented between the c) CP-FE simulation and the d) p-DIC measurement. The comparison is also presented on the cyan line profile between the e) CP-FE simulation and the f) p-DIC measurement.

The strain profiles obtained for CP-FE simulation (see Figure 11.c and e) reveal some strain heterogeneities with local maxima corresponding to strain bands. Like for the p-DIC measurements, these bands remained stable in space during the entire loading history.

The strain profiles along the vertical white line (see Figure 11.c and d) show a good correspondence between the CP-FE simulation results and the p-DIC measurements. Nonetheless, the simulated bands were sharper than the ones measured with p-DIC, with a width of around 40 µm and a higher ε_{zz} strain ratio inside and outside the bands: $\frac{\varepsilon_{zz}^{inside\ band}}{\varepsilon_{zz}^{outside\ band}} \in [1.3, 2.0]$. This may be attributed to higher spatial resolutions of the CP-FE simulation compared to the p-DIC method.

The strain profiles along the cyan line profile (see Figure 11.e and f) show poorer agreement between the simulation and experimental results. However, the band characteristics (width, spacing, strain ratio inside and outside the bands) are the same as for the white profile.

Finally, a quantitative comparison of the average strain ε_{zz} per grain obtained with CP-FE simulation and from p-DIC measurements was performed. Figure 12 summarizes the evolution over several load steps of this comparison for the three investigated slices y1, y2 and y3.

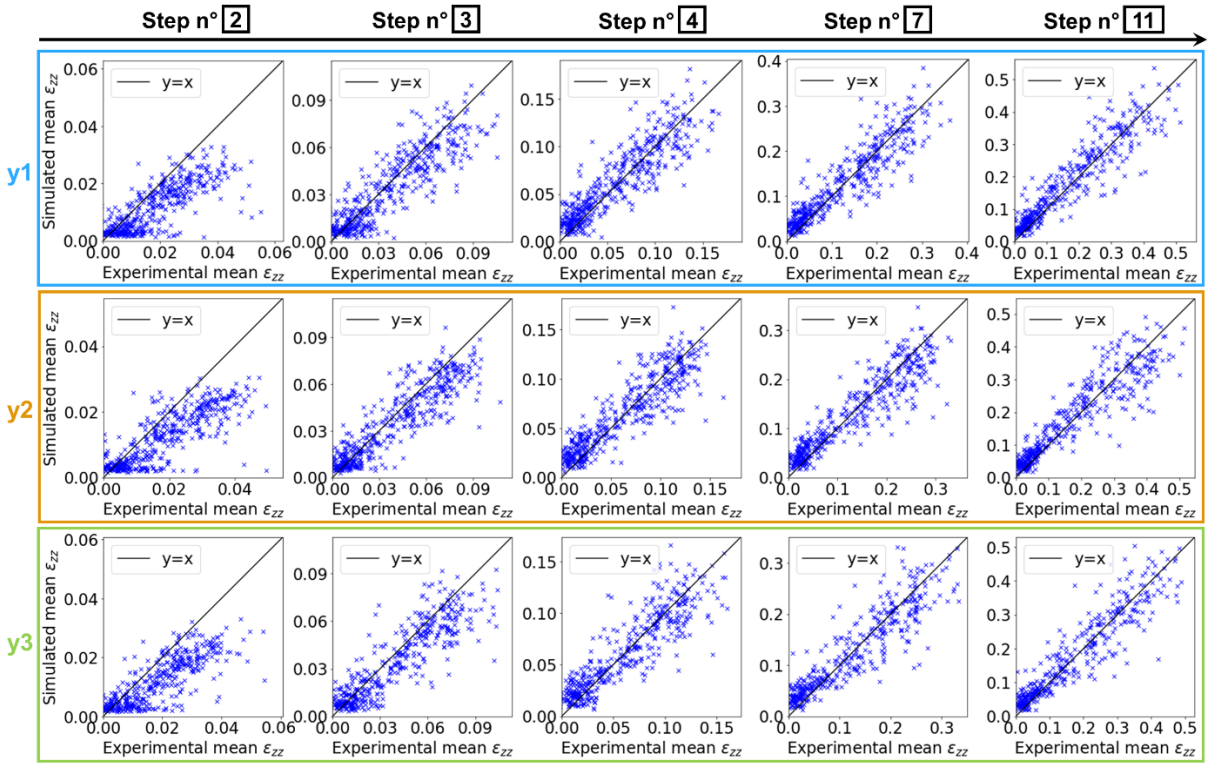

Figure 12 – Comparison of the simulated (CP-FE) and measured (p-DIC) average ε_{zz} per grain for the three slices y1, y2 and y3 investigated as it evolves over several load steps.

A strong correlation can be seen in the comparison trends, in particular from loading step 3 and onwards. The Pearson correlation coefficient was measured and it was found to increase with strain: at step 2, $r \in [0.73, 0.81]$ with $p < 1.10^{-84}$, at step 3, $r \in [0.87, 0.91]$ with $p < 1.10^{-142}$ and it slowly increased with strain up to step 11 where $r \in [0.92, 0.93]$ with $p < 1.10^{-172}$.

5. Discussion

A strain heterogeneity pattern in the form of spatially stable slanted bands was revealed by p-DIC measurements for the deformed 6016 T4 aluminium alloy. The heterogeneities developing at the beginning of plastic deformation were found to persist and continue to develop with straining, and to control the ultimate development of fracture. The fracture path systematically followed the bands of maximum strain. These results are in line with what was already observed for other aluminium alloys like AA2198 T8R (Morgeneyer et al., 2014), AA2198 T3 (Buljac et al., 2018), AA2139 T3 (Morgeneyer et al., 2016) and AA7075 T651 (Morgeneyer et al., 2021). The spatially stable bands are also in agreement with the findings of Kobayashi et al., who observed that grains deforming much at the onset of plasticity continue to do so (Kobayashi et al., 2022). A future work examining the crystallographic data acquired during this study is expected to lead to a better understanding of the factors responsible for the tendency of certain grains to deform more than others, based on different criteria like grain size or slip systems orientations.

It is important to distinguish between strain heterogeneity, which takes here the form of slanted strained bands, and strain localization bands. In the sense of continuum mechanics, localization bands indeed correspond to a situation where the deformation only occurs in the band and the material outside the band is no longer deformed plastically or is even unloaded. This is the step right before fracture. In the present study, the slanted strained bands observed from the early stages were strain heterogeneity since the material outside the bands continued to deform plastically. However, this heterogeneity seems to have been a precursor of the final strain localization and fracture since it occurred where there initially was a slanted strained band.

The heterogeneity measured for AA6016 T4, however, seems smaller than measured in previously investigated alloys. The ratio of the strain within the bands to that in the surrounding material was indeed measured to be between 1.2 and 1.7 whereas it was of the order of 1.5-2 for the other materials (Buljac et al., 2018; Morgeneyer et al., 2014, 2016) and even 2.5-3 for AA7075 T651 when strain localization occurred in the last loading steps (Morgeneyer et al., 2021). As already mentioned, a possible explanation for this difference in ratios could be the use of the Hencky strain, which is a logarithmic measure, in contrast to the Green-Lagrange strain used in the other studies. However, this logarithmic value does not alone explain the difference with the 2.5-3 ratio found for AA7075 T651. It is actually remarkable to find strain heterogeneity for such a material with high hardening capacity and small equiaxed grains inducing low to moderate anisotropy.

The origins of the experimentally measured slanted bands were investigated by performing numerical simulations. As anticipated, the macroscopic anisotropic plasticity model simulation did not reproduce the local strain heterogeneity, which motivated the study of the effects of polycrystalline microstructure. The originality of the current work lies in the non-destructive acquisition of the grain structure in the central ROI of the undeformed specimen. These data, acquired by lab-based DCT, were used as an input for 3D CP-FE simulations.

Multimodal experiments are more and more used to study deformation localization (Stinville et al., 2023) and are very promising but this comes with the challenge of data fusion that, if not carried out carefully, may yield wrong results and conclusions. Here, particular care was paid to managing the multiple error sources involved when using multimodal data. To enable a one-to-one comparison between p-DIC measurements and CP-FE simulations, a registration of DCT and ACT scans was performed as presented in section 2.4 by BSE and EBSD on a *post mortem* section with second phase particles used as fiducials for registration. The local frames to express the crystal orientations between EBSD, DCT and CP-FE were handled by means of the pymicro package (Marano et al., 2024). The *post*

mortem EBSD cross section appeared to be a valuable verification step and allowed building additional confidence in our findings.

In the end, the 3D CP-FE simulations reproduced the measured collective deformation behaviour of the polycrystalline aggregate very well. Hot spots are indeed in good agreement between the measured and simulated strain fields with the same magnitude of strain. A strong correlation is also found in the comparison of simulated and experimental average ε_{zz} per grain. These results suggest that polycrystalline effects are of first order importance for strain heterogeneity, which precedes strain localization and failure path. Whether another CP-FE model would have produced the same results was not tested in the present work but the authors assume that a properly calibrated CP-FE model would be able to reproduce the results. This could be investigated in future work.

It should be noted here that several factors affect the comparison between measured and simulated average strain values. Even if the microstructure is accurately described, discrepancies remain either from the lab-based DCT reconstructions or in the approximation made in the meshing step. Experimental measurements by p-DIC average the strain over a certain distance which can also introduce some errors. It was further verified – as presented in Figure 13 for slice y1 – that simulation results obtained with random orientations instead of those measured by DCT did not provide a similar strain field. This gives real confidence in using the CP-FE simulations to study strain localization at the scale of the grains.

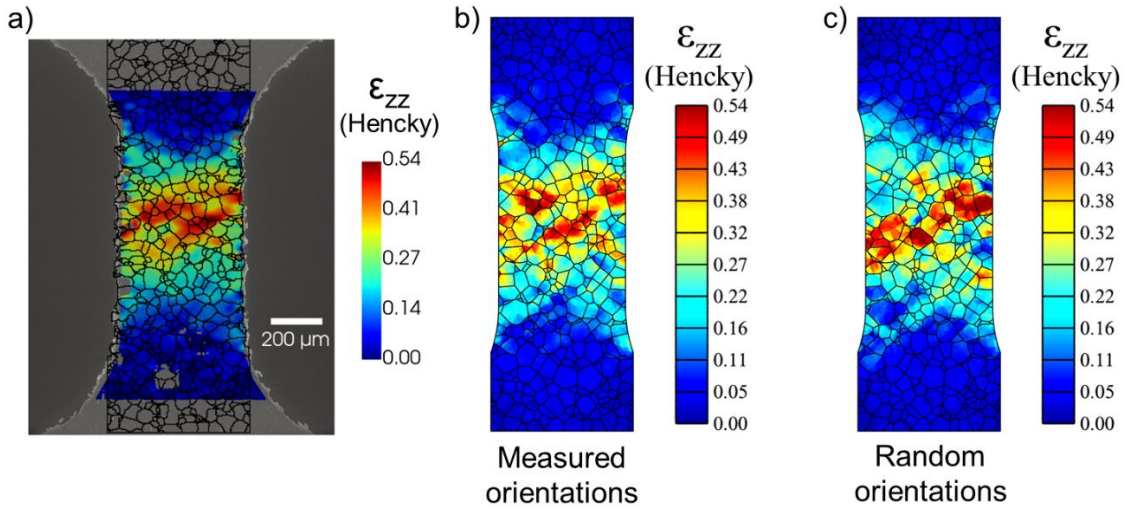

Figure 13 – Comparison of the internal accumulated strain field ε_{zz} in loading direction obtained for section y1 at step 11 with different methods: a) measured by p-DIC, b) calculated with 3D CP-FE with orientations measured by DCT and c) calculated with 3D CP-FE with random orientations drawn from the DCT measures. The Hencky strain fields are displayed in the reference configuration with the grain boundaries represented in black solid lines.

How various parameters like the grain size, shape or orientation independently affect the strain heterogeneity was investigated by Kobayashi et al. (Kobayashi et al., 2022), but no evident conclusion could be drawn. The strength of CP-FE simulations lies in their ability to address the complexity of the problem, by accounting for neighbouring effects. A longer-term perspective could be to use CP-FE simulations to understand the effect of microstructure (grain size, nature of grain boundaries, …) or micro-texture on macroscopic ductility and its anisotropy. The alloys' microstructure could then be tuned accordingly to optimize their formability.

The authors wish to draw attention to the importance of the choice of hardening parameters and boundary conditions for CP-FE simulations. The finite strains formalism as well as the identification of

hardening parameters up to large strain were found to be essential to reproduce the experimentally measured strain field. Also, applying the displacements calculated in the macroscopic simulation as boundary conditions for the CP-FE simulation helped a lot compared with more basic boundary conditions tested previously. Damage softening can also play a role at late stages of deformation. The physical damage evolution could be measured on the present data in a future work and a damage evolution rule may be included (Frodal et al., 2021).

As p-DIC was performed by taking advantage of the presence of more absorbing intermetallic particles, the measurement resolution was directly limited by the amount of visible particles. In the present study, the strain field was thus observed at the mesoscopic scale and could not be measured at the intragranular scale. However, by increasing the resolution of ACT scans, more intermetallic particles including smaller ones could be imaged, thus enabling higher-resolution strain field measurement. This could be achieved by using X-ray phase contrast nanotomography, which can reach a resolution of 50 nm (Hurst et al., 2023; Martinez-Criado et al., 2016).

6. Conclusion

This study finds for the first time strong correlations between measured internal strain field and CP-FE prediction on the 3D grain structure obtained by tomography. Taking advantage of correlative multimodal tomography data, the strain heterogeneities and their link with the polycrystalline structure have been investigated in a miniaturized plane strain tensile specimen made of AA6016 T4. The sample was first imaged non-destructively with lab-based DCT to provide the meshed grain structure used for 3D CP-FE simulations. ACT scans were then acquired in the same ROI during *in situ* loading, providing information of the internal contrast caused by intermetallic particles. Taking advantage of this natural speckle inside the material, p-DIC was performed, which in turn revealed early strain heterogeneities in form of slanted strained bands occurring before maximum load. Strain bands exhibiting the highest strains were observed to remain spatially stable and coincided with the final fracture location. The ratio of strain inside to outside the band was determined to be between 1.2 and 1.7 and the bands were found to be 70-80 µm wide and spaced from 100 to 150 µm. A macroscopic anisotropic plasticity model was found to not reproduce the measured heterogeneity, which motivated accounting for crystallographic effects through CP-FE simulations based on the real microstructure. 3D slabs of polycrystalline aggregates with three to four grains across the plane strain direction were meshed with the Neper software using Laguerre tessellation for three slices of interest inside the specimen based on the DCT scan information of the undeformed sample. The strain fields obtained by these experimentally driven CP-FE calculations were directly compared to those measured by p-DIC revealing a good match of hot spots and a similar strain magnitude. A strong statistical correlation was also found between the measured and CP-FE predicted average strain per grain in loading direction. This supports the hypothesis that crystallographic effects are responsible for early strain heterogeneities, which precede localization and the final failure path. It also promotes the use of CP-FE simulations based on the real arrangement of grain orientations to study the effects of grains on strain heterogeneity leading to localization and final fracture, for example to optimize aluminium alloy formability.

Acknowledgements

Constellium C-TEC, in particular Fanny Mas, is thanked for providing the material and for partially funding the study. Dr. Jean-Michel Scherer (Mines Paris) is thanked for his help with implementing the CP-FE simulations. The authors would also like to acknowledge Fabrice Gaslain (Mines Paris) for his help with EBSD acquisition and Djamel Missoum-Benziane (Mines Paris) for his help with the Z-set FE code and the development of post processing plugins.

Publication License

References

Arganda-Carreras, I., Sorzano, C.O.S., Marabini, R., Carazo, J.M., Ortiz-de-Solorzano, C., Kybic, J., 2006. Consistent and Elastic Registration of Histological Sections Using Vector-Spline Regularization, in: Beichel, R.R., Sonka, M. (Eds.), Computer Vision Approaches to Medical Image Analysis, Lecture Notes in Computer Science. Presented at the CVAMIA: Computer Vision Approaches to Medical Image Analysis, Springer, Berlin, Heidelberg, pp. 85–95. https://doi.org/10.1007/11889762_8

Ayres, R.A., Brazier, W.G., Sajewski, V.F., 1978. Evaluating the GMR-Limiting Dome Height Test as a new measure of press formability near plane strain. J. Applied Metalworking 1, 41–49. https://doi.org/10.1007/BF02833958

Bachmann, F., Bale, H., Gueninchault, N., Holzner, C., Lauridsen, E., 2019. 3D grain reconstruction from laboratory diffraction contrast tomography. J Appl Crystallogr 52. https://doi.org/10.1107/S1600576719005442

Bai, Y., Teng, X., Wierzbicki, T., 2009. On the Application of Stress Triaxiality Formula for Plane Strain Fracture Testing. Journal of Engineering Materials and Technology 131. https://doi.org/10.1115/1.3078390

Bao, Y., Wierzbicki, T., 2004. On fracture locus in the equivalent strain and stress triaxiality space. International Journal of Mechanical Sciences 46, 81–98. https://doi.org/10.1016/j.ijmecsci.2004.02.006

Barbe, F., Decker, L., Jeulin, D., Cailletaud, G., 2001. Intergranular and intragranular behavior of polycrystalline aggregates. Part 1: F.E. model. International Journal of Plasticity 17, 513–536. https://doi.org/10.1016/S0749-6419(00)00061-9

Bay, B.K., Smith, T.S., Fyhrie, D.P., Saad, M., 1999. Digital volume correlation: Three-dimensional strain mapping using X-ray tomography. Exp Mech 39, 217–226. https://doi.org/10.1007/BF02323555

Bean, C., Wang, F., Charpagne, M.A., Villechaise, P., Valle, V., Agnew, S.R., Gianola, D.S., Pollock, T.M., Stinville, J.C., 2022. Heterogeneous slip localization in an additively manufactured 316L stainless steel. International Journal of Plasticity 159, 103436. https://doi.org/10.1016/j.ijplas.2022.103436

Bornert, M., Chaix, J.-M., Doumalin, P., Dupré, J.-C., Fournel, T., Jeulin, D., Maire, E., Moreaud, M., Moulinec, H., 2004. Mesure tridimensionnelle de champs cinématiques par imagerie volumique pour l'analyse des matériaux et des structures. Instrumentation Mesure et Métrologie 4, 43–88. https://doi.org/10.3166/i2m.4.43-88

Bron, F., Besson, J., 2004. A yield function for anisotropic materials Application to aluminum alloys. International Journal of Plasticity 20, 937–963. https://doi.org/10.1016/j.ijplas.2003.06.001

Buljac, A., Hild, F., Helfen, L., Morgeneyer, T.F., 2018. On deformation and damage micromechanisms in strong work hardening 2198 T3 aluminium alloy. Acta Materialia 149, 29–45. https://doi.org/10.1016/j.actamat.2018.01.026

bUnwarpJ [WWW Document], 2020. . ImageJ Wiki. URL https://imagej.github.io/plugins/bunwarpj/index (accessed 3.5.24).

Frodal, B.H., Thomesen, S., Børvik, T., Hopperstad, O.S., 2021. On the coupling of damage and single crystal plasticity for ductile polycrystalline materials. International Journal of Plasticity 142, 102996. https://doi.org/10.1016/j.ijplas.2021.102996

Ganju, E., Nieto-Valeiras, E., LLorca, J., Chawla, N., 2023. A novel diffraction contrast tomography (DCT) acquisition strategy for capturing the 3D crystallographic structure of pure titanium. Tomography of Materials and Structures 1, 100003. https://doi.org/10.1016/j.tmater.2023.100003

Ghorbanpour, S., Alam, M.E., Ferreri, N.C., Kumar, A., McWilliams, B.A., Vogel, S.C., Bicknell, J., Beyerlein, I.J., Knezevic, M., 2020. Experimental characterization and crystal plasticity modeling

of anisotropy, tension-compression asymmetry, and texture evolution of additively manufactured Inconel 718 at room and elevated temperatures. International Journal of Plasticity 125, 63–79. https://doi.org/10.1016/j.ijplas.2019.09.002
Gille, M., Mas, F., Ehrström, J.-C., Daniel, D., 2024. Development of a plane strain tensile test to characterize the formability of 5xxx and 6xxx aluminium alloys. Int J Mater Form 17, 9. https://doi.org/10.1007/s12289-023-01805-9
Granum, H., Morin, D., Børvik, T., Hopperstad, O.S., 2021. Calibration of the modified Mohr-Coulomb fracture model by use of localization analyses for three tempers of an AA6016 aluminium alloy. International Journal of Mechanical Sciences 192, 106122. https://doi.org/10.1016/j.ijmecsci.2020.106122
Haldrup, K., Beckmann, F., Nielsen, S.F., Wert, J.A., 2008. Experimental determination of strain partitioning among individual grains in the bulk of an aluminium multicrystal. Materials Characterization 59, 842–851. https://doi.org/10.1016/j.matchar.2007.07.006
Han, X., 2012. Modélisation de la fragilisation due au gonflement dans les aciers inoxydables austénitiques irradiés (phdthesis). Ecole Nationale Supérieure des Mines de Paris.
Hartley, C.S., Kysar, J.W., 2020. Plane strain deformation by slip in FCC crystals. International Journal of Plasticity 133, 102842. https://doi.org/10.1016/j.ijplas.2020.102842
Héripré, E., Dexet, M., Crépin, J., Gélébart, L., Roos, A., Bornert, M., Caldemaison, D., 2007. Coupling between experimental measurements and polycrystal finite element calculations for micromechanical study of metallic materials. International Journal of Plasticity 23, 1512–1539. https://doi.org/10.1016/j.ijplas.2007.01.009
Holmberg, S., Enquist, B., Thilderkvist, P., 2004. Evaluation of sheet metal formability by tensile tests. Journal of Materials Processing Technology 145, 72–83. https://doi.org/10.1016/j.jmatprotec.2003.07.004
Hurst, M., Helfen, L., Morgeneyer, T.F., Suhonen, H., Buljac, A., Hild, F., Suuronen, J.-P., Baumbach, T., Hänschke, D., 2023. Hierarchically guided in situ nanolaminography for the visualisation of damage nucleation in alloy sheets. Sci Rep 13, 1055. https://doi.org/10.1038/s41598-022-27035-8
International Organization for Standardization, 2008a. ISO/DIS 12004-1, Metallic materials — Sheet and strip — Determination of forming-limit curves — Part 1: Measurement and application of forming-limit diagrams in the press shop.
International Organization for Standardization, 2008b. ISO/DIS 12004-2, Metallic materials — Sheet and strip — Determination of forming-limit curves — Part 2: Determination of forming-limit curves in the laboratory.
Johnson, G., King, A., Honnicke, M.G., Marrow, J., Ludwig, W., 2008. X-ray diffraction contrast tomography: a novel technique for three-dimensional grain mapping of polycrystals. II. The combined case. J Appl Cryst 41, 310–318. https://doi.org/10.1107/S0021889808001726
Kelly, P., 2013. Part I: An Introduction to Solid Mechanics - 4.2. Plane Strain, in: Solid Mechanics Lecture Notes. The University of Auckland, pp. 101–109.
Kobayashi, M., Zhang, Y., Ishikawa, H., Sun, J., Oddershede, J., Jensen, D.J., Miura, H., 2022. Relationships between 3D grain structure and local inhomogeneous deformation: A laboratory-based multimodal X-ray tomography investigation. Acta Materialia 240, 118357. https://doi.org/10.1016/j.actamat.2022.118357
Kong, X., Chen, J., Madi, Y., Missoum-Benziane, D., Besson, J., Morgeneyer, T., 2023. Plasticity and ductility of an anisotropic recrystallized AA2198 Al-Cu-Li alloy in T3 and T8 conditions during proportional and non-proportional loading paths: simulations and experiments. Journal of Theoretical, Computational and Applied Mechanics. https://doi.org/10.46298/jtcam.8913
Lankford, W.T., Snyder, S.C., Bauscher, J.A., 1950. New criteria for predicting the press performance of deep drawing sheets. Trans. ASM 42, 1197_1205.
Lin, F., Shi, Q., Delannay, L., 2020. Microscopic heterogeneity of plastic strain and lattice rotation in partially recrystallized copper polycrystals. International Journal of Solids and Structures,

Physics and Mechanics of Random Structures: From Morphology to Material Properties 184, 167–177. https://doi.org/10.1016/j.ijsolstr.2019.01.024
Lou, Y., Zhang, S., Yoon, J.W., 2020. Strength modeling of sheet metals from shear to plane strain tension. International Journal of Plasticity 134, 102813. https://doi.org/10.1016/j.ijplas.2020.102813
Ludwig, W., Schmidt, S., Lauridsen, E.M., Poulsen, H.F., 2008. X-ray diffraction contrast tomography: a novel technique for three-dimensional grain mapping of polycrystals. I. Direct beam case. J Appl Cryst 41, 302–309. https://doi.org/10.1107/S0021889808001684
Madec, R., Kubin, L.P., 2017. Dislocation strengthening in FCC metals and in BCC metals at high temperatures. Acta Materialia 126, 166–173. https://doi.org/10.1016/j.actamat.2016.12.040
Maire, E., Withers, P.J., 2014. Quantitative X-ray tomography. International Materials Reviews 59, 1–43. https://doi.org/10.1179/1743280413Y.0000000023
Marano, A., Ribart, C., Proudhon, H., 2024. Towards a data platform for multimodal 4D mechanics of material microstructures. Materials & Design 246, 113306. https://doi.org/10.1016/j.matdes.2024.113306
Martinez-Criado, G., Villanova, J., Tucoulou, R., Salomon, D., Suuronen, J.-P., Labouré, S., Guilloud, C., Valls, V., Barrett, R., Gagliardini, E., Dabin, Y., Baker, R., BOHIC, S., Cohen, C., Morse, J., 2016. ID16B: a hard X-ray nanoprobe beamline at the ESRF for nano-analysis. Journal of Synchrotron Radiation 23. https://doi.org/10.1107/S1600577515019839
Méric, L., Poubanne, P., Cailletaud, G., 1991. Single Crystal Modeling for Structural Calculations: Part 1—Model Presentation. Journal of Engineering Materials and Technology 113, 162–170. https://doi.org/10.1115/1.2903374
Mohr, D., Marcadet, S.J., 2015. Micromechanically-motivated phenomenological Hosford–Coulomb model for predicting ductile fracture initiation at low stress triaxialities. International Journal of Solids and Structures 67–68, 40–55. https://doi.org/10.1016/j.ijsolstr.2015.02.024
Morgeneyer, T.F., Khadyko, M., Buljac, A., Helfen, L., Hild, F., Benallal, A., Børvik, T., Hopperstad, O.S., 2021. On crystallographic aspects of heterogeneous plastic flow during ductile tearing: 3D measurements and crystal plasticity simulations for AA7075-T651. International Journal of Plasticity 144, 103028. https://doi.org/10.1016/j.ijplas.2021.103028
Morgeneyer, T.F., Taillandier-Thomas, T., Buljac, A., Helfen, L., Hild, F., 2016. On strain and damage interactions during tearing: 3D in situ measurements and simulations for a ductile alloy (AA2139-T3). Journal of the Mechanics and Physics of Solids 96, 550–571. https://doi.org/10.1016/j.jmps.2016.07.012
Morgeneyer, T.F., Taillandier-Thomas, T., Helfen, L., Baumbach, T., Sinclair, I., Roux, S., Hild, F., 2014. In situ 3-D observation of early strain localization during failure of thin Al alloy (2198) sheet. Acta Materialia 69, 78–91. https://doi.org/10.1016/j.actamat.2014.01.033
Nieto-Valeiras, E., Orozco-Caballero, A., Sarebanzadeh, M., Sun, J., LLorca, J., 2024. Analysis of slip transfer across grain boundaries in Ti via diffraction contrast tomography and high-resolution digital image correlation: When the geometrical criteria are not sufficient. International Journal of Plasticity 175, 103941. https://doi.org/10.1016/j.ijplas.2024.103941
Oddershede, J., Bachmann, F., Sun, J., Lauridsen, E., 2022. Advanced Acquisition Strategies for Lab-Based Diffraction Contrast Tomography. Integr Mater Manuf Innov 11, 1–12. https://doi.org/10.1007/s40192-021-00249-w
Ota, Y., Masuda, T., Kimura, S., 2020. Technical Trends in Aluminum Alloy Sheets for Automotive Body Panels. Kobelco Technology Review 16–20.
Papasidero, J., Doquet, V., Mohr, D., 2015. Ductile fracture of aluminum 2024-T351 under proportional and non-proportional multi-axial loading: Bao–Wierzbicki results revisited. International Journal of Solids and Structures 69–70, 459–474. https://doi.org/10.1016/j.ijsolstr.2015.05.006
Park, N., Stoughton, T.B., Yoon, J.W., 2020. A new approach for fracture prediction considering general anisotropy of metal sheets. International Journal of Plasticity 124, 199–225. https://doi.org/10.1016/j.ijplas.2019.08.011

Pelligra, C., Samei, J., Kang, J., Wilkinson, D.S., 2022. The effect of vanadium on microstrain partitioning and localized damage during deformation of unnotched and notched DP1300 steels. International Journal of Plasticity 158, 103435. https://doi.org/10.1016/j.ijplas.2022.103435

Pineau, A., Benzerga, A.A., Pardoen, T., 2016. Failure of metals I: Brittle and ductile fracture. Acta materialia 107, 424–483. https://doi.org/10.1016/j.actamat.2015.12.034

Proudhon, H., Herbig, M., Reischig, P., Buffiere, J.-Y., Ludwig, W., 2011. Simulation par éléments finis de la déformation de polycristaux à partir d'images de tomographie par contraste de diffraction, in: 10e Colloque National En Calcul Des Structures. Giens, France, p. 7 p.

Proudhon, H., Pelerin, M., King, A., Ludwig, W., 2020. In situ 4D mechanical testing of structural materials: The data challenge. Current Opinion in Solid State and Materials Science 100834. https://doi.org/10.1016/j.cossms.2020.100834

Quey, R., Dawson, P.R., Barbe, F., 2011. Large-scale 3D random polycrystals for the finite element method: Generation, meshing and remeshing. Computer Methods in Applied Mechanics and Engineering 200, 1729–1745. https://doi.org/10.1016/j.cma.2011.01.002

Quey, R., Renversade, L., 2017. Optimal polyhedral description of 3D polycrystals: method and application to statistical and synchrotron X-ray diffraction data. Computer Methods in Applied Mechanics and Engineering 330, 308–333. https://doi.org/10.1016/j.cma.2017.10.029

Renversade, L., Quey, R., 2024. Intra-grain orientation distributions in deformed aluminium: Synchrotron X-ray diffraction experiment and crystal-plasticity finite-element simulation. Acta Materialia 262, 119419. https://doi.org/10.1016/j.actamat.2023.119419

Rotella, J., Pilchak, A.L., Sangid, M.D., 2021. Examining the pathways for deformation band formation at the mesoscale. Materials Characterization 182, 111552. https://doi.org/10.1016/j.matchar.2021.111552

Roux, S., Hild, F., Viot, P., Bernard, D., 2008. Three-dimensional image correlation from X-ray computed tomography of solid foam. Composites Part A: Applied Science and Manufacturing, Full-field Measurements in Composites Testing and Analysis 39, 1253–1265. https://doi.org/10.1016/j.compositesa.2007.11.011

Rovinelli, A., Proudhon, H., Lebensohn, R.A., Sangid, M.D., 2020. Assessing the reliability of fast Fourier transform-based crystal plasticity simulations of a polycrystalline material near a crack tip. International Journal of Solids and Structures, Physics and Mechanics of Random Structures: From Morphology to Material Properties 184, 153–166. https://doi.org/10.1016/j.ijsolstr.2019.02.024

Sarmah, A., Asqardoust, S., Jain, M.K., Yuan, H., 2024. 3D microstructure-based modelling of ductile damage at large plastic strains in an aluminum sheet. International Journal of Plasticity 181, 104088. https://doi.org/10.1016/j.ijplas.2024.104088

Sedighiani, K., Shah, V., Traka, K., Diehl, M., Roters, F., Sietsma, J., Raabe, D., 2021. Large-deformation crystal plasticity simulation of microstructure and microtexture evolution through adaptive remeshing. International Journal of Plasticity 146, 103078. https://doi.org/10.1016/j.ijplas.2021.103078

Singh, J., Kim, M.-S., Choi, S.-H., 2019. The effect of initial texture on micromechanical deformation behaviors in Mg alloys under a mini-V-bending test. International Journal of Plasticity, Ductility Enhancement: Advances in Experimental and Computational Micromechanics - In Honor of Dr. Raja K. Mishra 117, 33–57. https://doi.org/10.1016/j.ijplas.2018.01.008

Stinville, J.-C., Charpagne, M.-A., Maaß, R., Proudhon, H., Ludwig, W., Callahan, P.G., Wang, F., Beyerlein, I.J., Echlin, M.P., Pollock, T.M., 2023. Insights into Plastic Localization by Crystallographic Slip from Emerging Experimental and Numerical Approaches. Annual Review of Materials Research 53, 275–317. https://doi.org/10.1146/annurev-matsci-080921-102621

Sutton, M.A., Orteu, J.-J., Schreier, H., 2009. Image correlation for shape, motion and deformation measurements: basic concepts, theory and applications, Springer US. ed.

Tasan, C.C., Diehl, M., Yan, D., Zambaldi, C., Shanthraj, P., Roters, F., Raabe, D., 2014. Integrated experimental–simulation analysis of stress and strain partitioning in multiphase alloys. Acta Materialia 81, 386–400. https://doi.org/10.1016/j.actamat.2014.07.071

The Aluminum Association, 2018. International Alloy Designations and Chemical Composition Limits for Wrought Aluminum and Wrought Aluminum Alloys: Teal Sheet (No. ISSN : 2377-6692).

Thomason, P.F., 1990. Ductile fracture of metals, 1st ed. ed. Pergamon Press, Oxford [England] New York.

Vallin, J., Mongy, M., Salama, K., Beckman, O., 2004. Elastic Constants of Aluminum. Journal of Applied Physics 35, 1825–1826. https://doi.org/10.1063/1.1713749

Vaughan, M.W., Lim, H., Pham, B., Seede, R., Polonsky, A.T., Johnson, K.L., Noell, P.J., 2024. The mechanistic origins of heterogeneous void growth during ductile failure. Acta Materialia 274, 119977. https://doi.org/10.1016/j.actamat.2024.119977

Watarai, H., 2006. Trends of research and development for magnesium alloys - Reducing the weight of structural materials in motor vehicles. Science and Technology Trends 84–97.

Wu, S.C., Xiao, T.Q., Withers, P.J., 2017. The imaging of failure in structural materials by synchrotron radiation X-ray microtomography. Engineering Fracture Mechanics 182, 127–156. https://doi.org/10.1016/j.engfracmech.2017.07.027

Xiao, C., Sun, R., Adrien, J., Lachambre, J., Nadot, Y., Weck, A., Buffière, J.-Y., 2024. 3D characterization of closure of surface and internal fatigue cracks in nodular cast iron using Digital Volume Correlation of laboratory X-ray tomography images. International Journal of Fatigue 182, 108226. https://doi.org/10.1016/j.ijfatigue.2024.108226

Zhao, Z., Ramesh, M., Raabe, D., Cuitiño, A.M., Radovitzky, R., 2008. Investigation of three-dimensional aspects of grain-scale plastic surface deformation of an aluminum oligocrystal. International Journal of Plasticity 24, 2278–2297. https://doi.org/10.1016/j.ijplas.2008.01.002

Z-set, 2022. Z-set | Non-linear material & structure analysis suite [WWW Document]. URL http://www.zset-software.com/

Appendices

A. Macroscopic anisotropic plasticity model and identification of parameters

The yield surface proposed by Bron et al. (Bron and Besson, 2004) is expressed as follows:

$$\phi = \bar{\sigma} - R(p)$$

$\bar{\sigma}$ is an equivalent stress defined as follows:

$$\bar{\sigma} = (\alpha {\bar{\sigma}_1}^a + (1-\alpha){\bar{\sigma}_2}^a)^{1/a}$$

$$\bar{\sigma}_1 = \left(\frac{1}{2}\left(\left|S_2^1 - S_3^1\right|^a + \left|S_3^1 - S_1^1\right|^a + \left|S_1^1 - S_2^1\right|^a\right)\right)^{1/a}$$

$$\bar{\sigma}_2 = \left(\frac{3^a}{2^a+2}\left(\left|S_1^2\right|^a + \left|S_2^2\right|^a + \left|S_3^2\right|^a\right)\right)^{1/a}$$

where α and a are two material parameters influencing the shape of the yield surface and $S_{i=1-3}^k$ are the principal values of a modified stress deviator $\underset{\sim}{s}^k$:

$$\underset{\sim}{s}^k = \underset{\approx}{L}^k : \underset{\sim}{\sigma}$$

$$\underset{\approx}{L}^k = \begin{pmatrix} (c_2^k + c_3^k)/3 & -c_3^k/3 & -c_2^k/3 & 0 & 0 & 0 \\ -c_3^k/3 & (c_3^k + c_1^k)/3 & -c_1^k/3 & 0 & 0 & 0 \\ -c_2^k/3 & -c_1^k/3 & (c_1^k + c_2^k)/3 & 0 & 0 & 0 \\ 0 & 0 & 0 & c_4^k & 0 & 0 \\ 0 & 0 & 0 & 0 & c_5^k & 0 \\ 0 & 0 & 0 & 0 & 0 & c_6^k \end{pmatrix}$$

c_5^k and c_6^k are set to 1 as the work focuses on thin sheets.

$R(p)$ corresponds to the non linear isotropic hardening expressed as a function of the accumulated plastic strain p:

$$R(p) = R_O\left[1 + K_1\left(1 - e^{-b_1 p}\right) + K_2\left(1 - e^{-b_2 p}\right)\right]$$

where R_O is the yield strength, K_1 and K_2 the hardening capacities and b_1 and b_2 the hardening speeds.

The material parameters were identified by optimization on single element calculations to reproduce experimental data from uniaxial tensile (UT) tests that were performed in seven different directions ranging from the rolling direction L to the transverse direction T. First, the hardening parameters were estimated only by considering the stress response of the UT test in the rolling direction with a Von Mises yield criterion. Then, the hardening parameters were fixed, and the plastic anisotropy parameters were estimated through an optimization on the seven UT tests both in terms of stress and plastic strain (Lankford coefficients) response. A final optimization step on the seven UT tests enabled refining the identification of the hardening and plastic anisotropy parameters that are given in Table A. 1 and Table A. 2 respectively. Figure A. 1 shows a comparison of the UT experimental data with the simulated results using the identified model.

R_0 (MPa)	K_1	b_1	K_2	b_2
62.93	0.48	381.64	2.34	7.46

Table A. 1 – Identified hardening parameters

a	α	c_1^1	c_2^1	c_3^1	c_4^1	c_5^1	c_6^1	c_1^2	c_2^2	c_3^2	c_4^2	c_5^2	c_6^2
12	0.5	0.944	0.884	0.522	0.719	1.0	1.0	0.623	0.595	0.986	0.830	1.0	1.0

Table A. 2 – Identified plastic anisotropy parameters

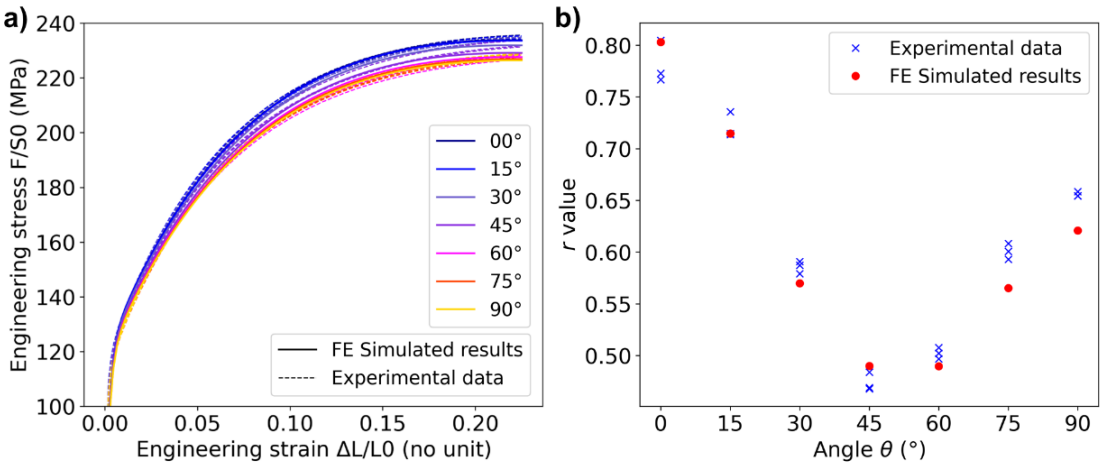

Figure A. 1 – Comparison of UT experimental data and FE simulated results after optimization of the parameters of the Bron-Besson model: a) stress versus strain (note: the y-axis starts at 100 MPa for a

better visibility of the curves); b) Lankford coefficients r for the different tested directions of the metal sheet.

The relevance of the identified parameters was verified by comparing the model's predictions with available experimental data for different types of specimens including notched tension (NT6 and NT20), central hole (CH) and shear (SH). As shown on Figure A. 2, the calculated predictions were found to be very close to experimental data.

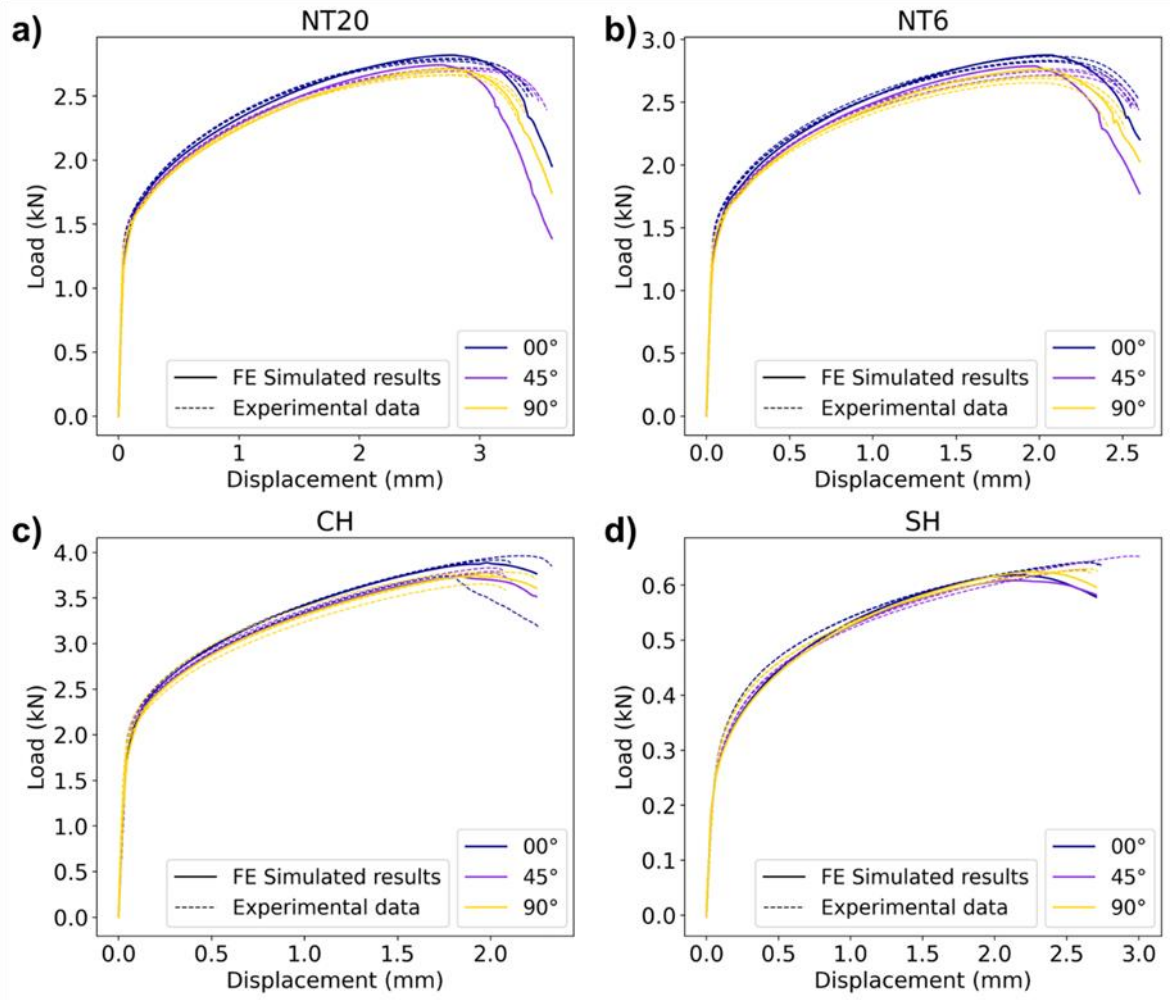

Figure A. 2 – Comparison of experimental (dashed lines) and numerically-predicted (solid lines) load-displacement curves for 4 specimen geometries: a) NT20, b) NT6, c) CH and d) SH. For each geometry, 3 directions of the metal sheet are tested: 0°: rolling, 45°: diagonal and 90°: transverse.

B. Experimental plane strain validation

The specimen geometry, designed with the help of FE simulations, was validated experimentally by means of a tensile test instrumented with DIC. A speckle was applied with an airbrush on the surface of the specimen and images were acquired continuously with a frequency of 1 Hz during the tensile test with pin displacement speed of 2 µm/s. The strain field was measured with the VIC-2D software from Correlated Solution. Subset size was 75 pixels corresponding to 141 µm, step size was 10 pixels and Lagrange strain was measured with filter size 15. The measured $\left|\varepsilon_{zz}/\varepsilon_{yy}\right|$ field is displayed on Figure B. 1 for two instants of the test. As soon as plasticity occurs, the central ROI was found to be in plane strain as it verified the fixed criterion $\left|\varepsilon_{zz}/\varepsilon_{yy}\right| > 10$, and fracture initiated in this area, which validated the specimen geometry.

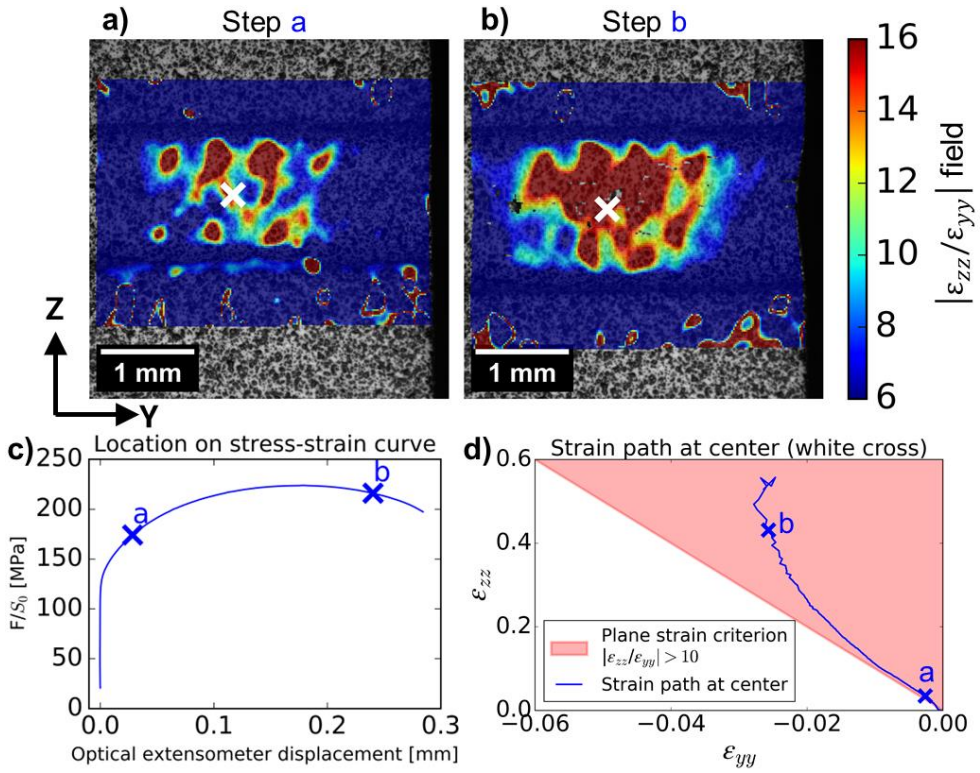

Figure B. 1 – $|\varepsilon_{zz}/\varepsilon_{yy}|$ field obtained with surface DIC on the miniaturized plane strain tension specimen for a) step a and b) step b as described on the c) mechanical stress-strain curve; d) the strain path at the center of the specimen (defined by a white cross on figures a and b) verifies the plane strain criterion: $|\varepsilon_{zz}/\varepsilon_{yy}| > 10$.

C. Material parameters identification for CP-FE simulation

The identification of material parameters was carried out by optimizing the macroscopic response of a polycrystalline aggregate under uniaxial tension compared to experimental data. Following a convergence analysis, an aggregate of 125 cubic grains with 8 elements per grain was chosen. Random crystallographic orientations drawn from the DCT measurement, and thus representative of the material texture, were assigned to the cubic grains. Reduced quadratic hexahedral elements (c3d20r) were used for the simulation.

The identification was performed in three steps:

- A first estimation of the hardening parameters τ_0, Q, b, c and d was obtained by fixing the viscosity parameters to $K = 5\ MPa.s^{1/n}$ and $n = 5$. A unique strain rate of $\dot{\varepsilon} = 1.10^{-3}\ s^{-1}$ was considered.
- Then, the optimized τ_0, Q, b, c and d were fixed and viscosity parameters K and n were identified based on experimental data at two strain rates: $\dot{\varepsilon} = 1.10^{-3}\ s^{-1}$ and $\dot{\varepsilon} = 2.5.10^{-4}\ s^{-1}$.
- Finally, the identified viscosity parameters K and n were fixed to refine the optimization of hardening parameters τ_0, Q, b, c and d, only considering the strain rate: of $\dot{\varepsilon} = 1.10^{-3}\ s^{-1}$.

Figure C. 1 presents the comparison of the stress-strain curve simulated for the aggregate with optimized parameters (black lines) with the experimental data (colored crosses). The simulated curves match well the experimental data, but the comparison is only available for strains up to 25 % as there is no available experimental data beyond this point.

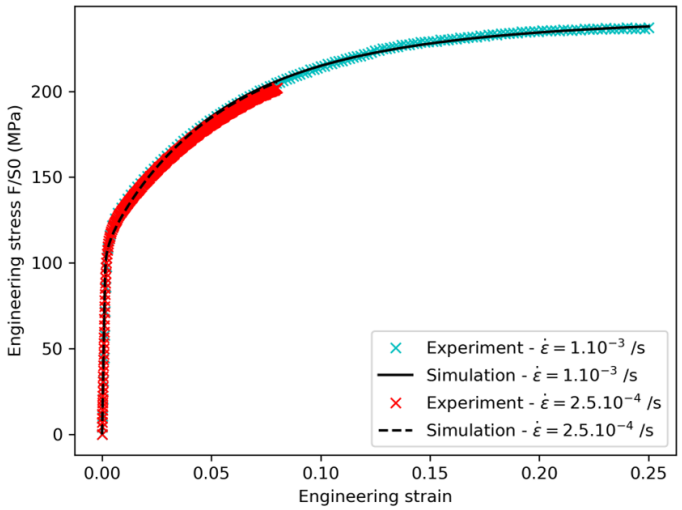

Figure C. 1 – Validity assessment of identified material parameters for CP-FE simulations: comparison of the CP-FE-simulated macroscopic response of a 125-grain aggregate (black lines) with experimental data (colored crosses) for two different strain rates

D. Damage measurement

The damage evolution was measured using the high-resolution ACT scans. This for, a same parallelepiped volume located in the core of the specimen and covering 352.8 x 680.8 x 332.8 µm^3 on the initial scan was tracked. The grey levels contained in this sub-volume were then segmented using a region growing method, with two "seed" and "growth" thresholds, to identify the voxels corresponding to porosities. As greyscale distributions vary from one scan to another, seed and growth thresholds were determined manually for each scan with help of Fiji. The accuracy of the segmentation method depending essentially on the choice of the thresholds and the images being coded on 16 bits, i.e. with 65536 grey levels, it was determined by eye that the error on the chosen thresholds was ±150. To evaluate the measurement error, two "boundary" cases were therefore segmented for each scan with thresholds decreased and increased by 150. The void volumic content was then simply measured as the ratio of the volume of detected porosities over the total volume of the scan. Its evolution is shown on Figure D. 1, where one can see that the damage only increases from step 7 and remains rather low.

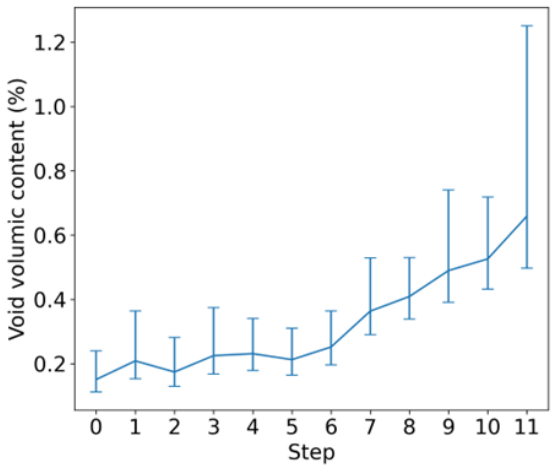

Figure D. 1 – Evolution of the void volumic content in the core of the plane strain tensile specimen. The error bars result from measurements performed on scans segmented with thresholds at ± 150 out of the 65536 grey levels on which the images are coded.

E. Verification of the plane strain condition on the polycrystal simulation

The boundary conditions imposed on the meshed polycrystalline aggregates being prescribed from the specimen simulation, a verification has been made here to determine how close the three simulated polycrystalline aggregates around y1, y2 and y3 are to plane strain. To this end, two extensometers defined in Figure E. 1.a were used to measure the deformation of the central ROI of the polycrystalline aggregates along Y and Z. The such measured strain paths are shown on Figure E. 1.b, all verifying the plane strain criterion of $|\varepsilon_{zz}/\varepsilon_{yy}| > 10$. As expected, the polycrystalline aggregate around y2, which is closer to the core of the specimen, is closer to perfect plane strain with $\varepsilon_{yy} = -1.42\ \%$ at the end of the simulation while it is of $-1.76\ \%$ and $-1.96\ \%$ for aggregates around y1 and y3 respectively.

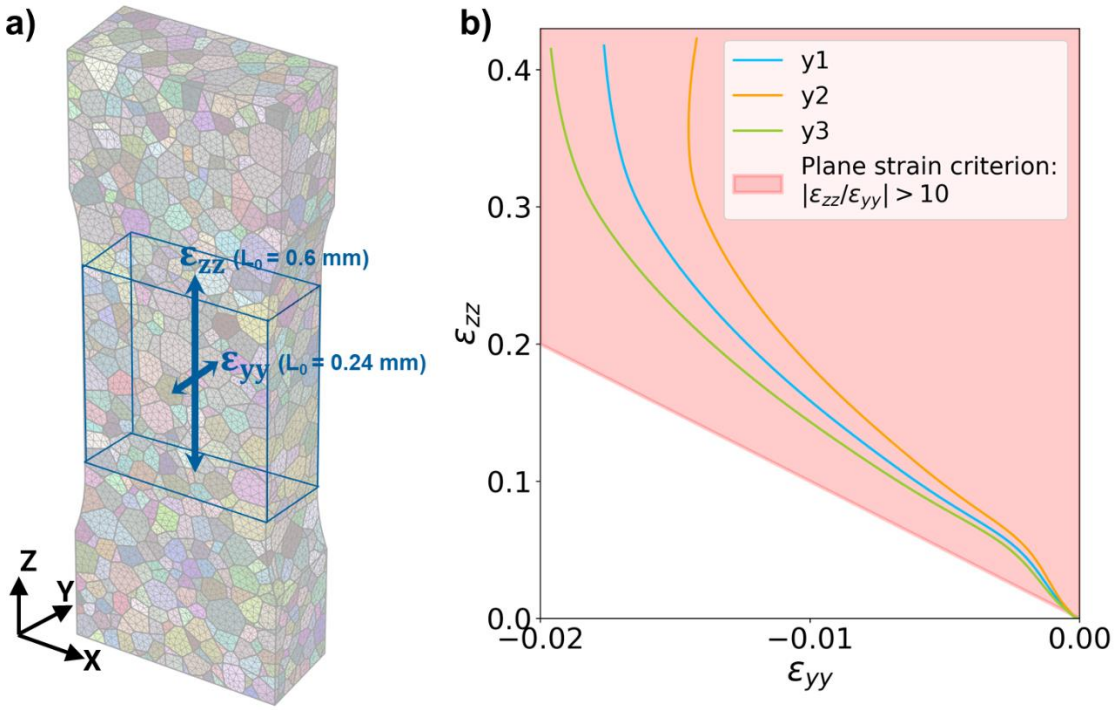

Figure E. 1 – Verification of the plane strain condition on the three polycrystal CP-FE simulations: a) definition of the extensometers used to assess the deformation of the central ROIs of the simulated aggregates; b) strain paths of the ROIs of the three polycrystal CP-FE simulations around y1, y2 and y3.